M/NEM DEVICES AND UNCERTAINTY QUANTIFICATION

BY

NAMJUNG KIM

DISSERTATION

Submitted in partial fulfillment of the requirements
for the degree of Doctor of Philosophy in Theoretical and Applied Mechanics
in the Graduate College of the
University of Illinois at Urbana-Champaign, 2018

Urbana, Illinois

Doctoral Committee:

Professor Narayana R. Aluru, Chair
Professor Placid M. Ferreira
Professor Shiv G. Kapoor
Professor Rohit Bhargava
Assistant Professor Seok Kim

Abstract

Recent advances in computing power have facilitated the use of computational simulations as design guidelines in a range of fields including the semiconductor industry, biosensors, microfluidic devices, and even nano-sized devices. Although simulation can capture the physics behind the experiment, deterministic simulations with parameters derived from least-square fitting are significantly limited for understanding output distributions from experiments. This deviation between computational simulation and experiment may arise for a number of reasons: the stochastic nature of design parameters, external environmental fluctuations, measurement noise, and so forth. These are called uncertainties. Understanding the effect of these uncertainties is important in manufacturing processes, because manufacturing processes incorporate multi-scale and multi-physics sub-steps, with uncertainties in inputs accumulated and propagated through the sub-steps, resulting in significant deviations in the performance of final products.

A systematic approach to understanding the variations in the output from various uncertainty sources is called uncertainty quantification (UQ). To integrate uncertainty quantification fully into the design process, the sources of uncertainty must be identified and quantified; then, the uncertainty needs to be characterized and parameterized to create a statistical model. The parameterized statistical model is fed into a physics-based deterministic model (e.g., a finite element model) to quantify the deviations in the final products arising from the uncertainty parameters. By understanding the effect of stochastic parameters in inputs as well as manufacturing processes, computational simulations can provide more reliable design guidelines across a range of manufacturing fields.

This dissertation consists of two parts. The first part describes how simulation can assist in understanding experimental results. The specific physical systems considered in this dissertation are a MEMS-based resonator (Chapter 2) and a microfluidic device (Chapter 3). The results show that simulation is a powerful tool for describing details of experimental results that cannot be explained easily due to the complexity of the systems. However, distinctive discrepancies between the results from current computational predictions and experiments still exist, especially when various uncertainties are present. Therefore, the second part of this dissertation is devoted to developing a systematic approach to modeling stochastic input variables through experimental data, and describing how this can be incorporated into a modeling framework.

This dissertation suggests a systematic approach to developing a finite element model that can estimate the mechanical properties of final products with spatial uncertainties in the 3D printing process (Chapter 4), and those arising from variations in microstructure in the die-casting process (Chapter 5). Those input uncertainties are extracted from the images of final products. The data-driven modeling approach with Gaussian process is proposed to consider the probabilistic behavior of uncertainties. The realizations sampled from the calibrated Gaussian process model are incorporated into the deterministic model, generating more realistic simulation model. The systematic approach developed in this study can assist in understanding the effect of input uncertainties on the variance of the mechanical performance of final products from 3D printing and die-casting. This approach will be beneficial to other manufacturing processes where input uncertainties are important.

Table of Contents

Chapter 1

Introduction

Recent advances in computing power have facilitated the use of computational simulations as design guidelines in a range of fields including the semiconductor industry,[1] biosensors,[2] microfluidic devices,[3] and even nano-sized devices.[4] Recently, computer simulations have been used to explore the possible applications of forces that have been proved theoretically but not yet measured, due to their extremely small magnitudes.[5] Computer simulation has also been applied to the investigation of poorly-understood mechanisms underlying cell cycle progression.[6] Currently, simulations can assist in understanding a wide range of systems, from mechanical behaviors of a single cell to entire manufacturing processes. As increasing the complexity of the system, computer simulations require consideration of phenomena across multiple scales and multiple physical fields.

However, significant discrepancies between the results of computational predictions and experimental data still frequently exist. This deviation between computational simulation and experiment may arise for a number of reasons: 1) lack of understanding of the nature of the problem; 2) errors from over-simplification of the problem; 3) accumulated computational errors during calculation; 4) measurement errors; and 5) the stochastic nature of physical phenomena. This unexpected deviation between simulation and experiment is called output uncertainty. The multiple sources of output uncertainty can be systematically categorized as either epistemic uncertainties or aleatoric uncertainties.[7] Epistemic uncertainties arise from uncertainty that comes from lack of knowledge, and can be reduced by increased understanding of physical phenomena, improved estimation of input parameters, and the accuracy of the computational model. However, aleatoric uncertainties originate from the

inherent stochasticity of the problem: the stochastic nature of design parameters, external environmental fluctuations, measurement noise, and so forth. These errors cannot be easily eradicated in experiments, nor simulated using a traditional computational model, unless the inherent stochasticity of the problem is fully understood. If a manufacturing process consists of multiple steps with multiple physical phenomena and multiple scales, these uncertainties in inputs accumulate and propagate through the steps, resulting in significant deviations in the performance of the final products. This cannot be captured in deterministic simulations.

A systematic approach to understanding discrepancies between simulation and experimental results is called uncertainty quantification (UQ). Initially, UQ gained attention in a range of areas where higher manufacturing tolerances are required, such as micro- or nano-electromechanical systems (M/NEMS).[8] Later, UQ became important even in traditional manufacturing process, such as die casting, because it is useful for understanding the effect of uncertainties in process parameters. UQ can be further used to create a priority list of input uncertainties to be controlled through sensitivity analysis[9] and time-dependent reliability analysis.[10] Recently, as additive manufacturing processes have been more widely used to make structural parts and large numbers of products,[11] UQ has become a necessity for obtaining consistent quality control. By understanding the effect of stochastic parameters in inputs as well as manufacturing processes, computational simulations can provide more reliable design guidelines across a range of manufacturing fields.

To integrate uncertainty quantification fully into the design process, the sources of uncertainty must be identified and quantified; then, the uncertainty needs to be characterized and parameterized to create a statistical model. The parameterized statistical model is fed into a physics-based deterministic model (e.g., a finite element model) to quantify the deviations in the final products arising from the uncertainty parameters. Without UQ, device designs must be sufficiently robust to tolerate deviations in fabrication processes, and a large number of

unnecessary margins or safety factors are required to guarantee the performance of final devices within certain tolerances.

This dissertation consists of two parts. The first part describes how simulation can assist in understanding experimental results. The specific physical systems considered in this dissertation are a MEMS-based resonator (Chapter 2) and a microfluidic device (Chapter 3). The results show that simulation is a powerful tool for describing details of experimental results that cannot be explained easily due to the complexity of the systems. Although simulation can capture the physics behind the experiment, deterministic simulations with parameters derived from least-square fitting are significantly limited for understanding output distributions from experiments. Therefore, the second part of this dissertation suggests a systematic approach to understanding the effects of various stochastic uncertainties in inputs on the system output. This work mainly considers two uncertainties: spatial uncertainty in geometrical shapes (Chapter 4) and inhomogeneity in material properties from microstructures (Chapter 5).

In Chapter 2, a computational model is used to understand the mass reading from a MEM-based resonator that measures the mass of a target cell attached to the surface of the resonator. Because the resonant frequency of the resonator is inversely proportional to the square root of its total mass, the mass of the target cell can be calculated by measuring a shift in the resonant frequency of the resonator before and after the target is attached. This is valid when the stiffness of the target entity is infinite: the vibration phase of the target is exactly matched with the resonator. However, when the stiffness of the target is finite, the mass reading from the frequency shift often under-predicts the target mass. This phenomena is called the "missing mass effect[12]". In this chapter, we suggest a computational model that can assist in understanding the effect of the finite stiffness of the target entity. In addition, various cases that can change the mass reading, such as the position of the target and the shape of the target,

are systematically studied and the effects quantified. The results assist in understanding the mass readings of cells attached to the resonator.

In Chapter 3, a numerical model is used to understand the mixing behavior of two fluids inside a 3D helical micromixer. A traditional micromixer has a low mixing rate because the flow inside the channel is in the laminar flow regime.[13] However, a round-channel helical mixer enhances the mixing rate by inducing a transverse secondary flow inside the channel, called the Dean effect.[14] By using a freeform 3D printed sacrificial template and stimulated Raman scattering microscopy, 3D chemical images of the mixing of glucose and saltwater in a full 3D helical micromixer are presented.[15] To validate and quantify the mixing phenomena measured in the experiment, the mixing behavior of two fluids inside the channel is calculated through a computational model. The result confirms that the observed experiment results are consistent with the analytical prediction. In addition to this validation, the mixing performance of the helical mixer is compared with that of a commonly-used staggered, herringbone mixer.[16] Based on the mixing performance quantified in the numerical model, above a certain Reynolds number, the helical mixer outperforms an optimized herringbone mixer in terms of pressure drop, mixing volume, and mixing time. This work can also be used as a design guideline for optimizing the shape of a helical mixer.

Chapter 4 suggests a systematic UQ approach for development of a finite element model that can estimate the mechanical properties of 3D printed unit cells with spatial uncertainties. The spatial uncertainties in this chapter are defined as the geometrical difference between the actual printed geometry (stair-like sidewall profile) and the planned geometry (CAD geometry). The spatial uncertainties are extracted from images of the sidewall profile of 3D printed struts at different printing angles. A data-driven modeling approach with a Gaussian process (GP) is proposed to consider the probabilistic behavior of spatial uncertainties in the printing process. The realizations sampled from the GP model are incorporated into the

planned geometry, generating a more realistic simulation model. A simulation of a uniaxial compression test is performed on the unit cell geometries to understand the effect of spatial uncertainties. The results show that spatial uncertainties can significantly affect the mechanical properties of 3D printed unit cells under compressive loading conditions. In addition, these effects become more important when the relative density of the cellular structure decreases, because the length scale of spatial uncertainties becomes comparable or dominant as the size of the unit cell structure decreases.

In Chapter 5, an "input parameters-manufacturing process-product property" framework with UQ is suggested, which helps in understanding the distribution of mechanical properties of die-casting products. The "input parameters-manufacturing process-product property" framework represents a computational approach that can connect input parameters with final product quality through manufacturing process modeling. Within this framework, a novel characterization method that can extract microstructural information (e.g., grain size) from experimental micrographs is developed. This dissertation also proposes a calibration/validation framework that increases the reliability of the computational model by incorporating experimental data. The stochasticity of microstructures is modeled efficiently by including the GP model in the computational framework. Additionally, Bayesian inference is used to estimate parameters in the GP model. A highly reliable computational framework is achieved by feeding the experimental data into the calibration/validation framework. The proposed framework provides a general methodology that assists in calibrating and validating the computational model that simulates the entire manufacturing process, with uncertainties.

1.1 References

1. Selberherr, S., *Analysis and simulation of semiconductor devices*. Springer Science & Business Media: 2012.

2. (a) Wang, J., Carbon-nanotube based electrochemical biosensors: A review. *Electroanalysis* **2005,** *17* (1), 7-14; (b) Shao, Y.; Wang, J.; Wu, H.; Liu, J.; Aksay, I. A.; Lin, Y., Graphene based electrochemical sensors and biosensors: a review. *Electroanalysis* **2010,** *22* (10), 1027-1036; (c) Fan, X.; White, I. M.; Shopova, S. I.; Zhu, H.; Suter, J. D.; Sun, Y., Sensitive optical biosensors for unlabeled targets: A review. *analytica chimica acta* **2008,** *620* (1), 8-26.

3. (a) Lee, C.-Y.; Chang, C.-L.; Wang, Y.-N.; Fu, L.-M., Microfluidic mixing: a review. *International journal of molecular sciences* **2011,** *12* (5), 3263-3287; (b) Gravesen, P.; Branebjerg, J.; Jensen, O. S., Microfluidics-a review. *Journal of Micromechanics and Microengineering* **1993,** *3* (4), 168.

4. (a) Rhoads, J. F.; Shaw, S. W.; Turner, K. L., Nonlinear dynamics and its applications in micro-and nanoresonators. *Journal of Dynamic Systems, Measurement, and Control* **2010,** *132* (3), 034001; (b) Batra, R.; Porfiri, M.; Spinello, D., Review of modeling electrostatically actuated microelectromechanical systems. *Smart Materials and Structures* **2007,** *16* (6), R23.

5. (a) Georgescu, I.; Ashhab, S.; Nori, F., Quantum simulation. *Reviews of Modern Physics* **2014,** *86* (1), 153; (b) Corona-Ugalde, P.; Martín-Martínez, E.; Wilson, C.; Mann, R. B., Dynamical Casimir effect in circuit QED for nonuniform trajectories. *Physical Review A* **2016,** *93* (1), 012519.

6. Park, K.; Millet, L. J.; Kim, N.; Li, H.; Jin, X.; Popescu, G.; Aluru, N.; Hsia, K. J.; Bashir, R., Measurement of adherent cell mass and growth. *Proceedings of the National Academy of Sciences* **2010,** *107* (48), 20691-20696.

7. (a) Sullivan, T. J., *Introduction to uncertainty quantification*. Springer: 2015; Vol. 63;

(b) Coleman, H. W.; Steele, W. G., *Experimentation, validation, and uncertainty analysis for engineers*. John Wiley & Sons: 2009.

8. (a) Agarwal, N.; Aluru, N., Stochastic modeling of coupled electromechanical interaction for uncertainty quantification in electrostatically actuated MEMS. *Computer Methods in Applied Mechanics and Engineering* **2008,** *197* (43), 3456-3471; (b) Agarwal, N.; Aluru, N. R., A domain adaptive stochastic collocation approach for analysis of MEMS under uncertainties. *Journal of Computational Physics* **2009,** *228* (20), 7662-7688; (c) Agarwal, N.; Aluru, N., A data-driven stochastic collocation approach for uncertainty quantification in MEMS. *International Journal for Numerical Methods in Engineering* **2010,** *83* (5), 575-597; (d) Alwan, A.; Aluru, N., Uncertainty quantification of MEMS using a data-dependent adaptive stochastic collocation method. *Computer Methods in Applied Mechanics and Engineering* **2011,** *200* (45), 3169-3182.

9. Liang, B.; Mahadevan, S., Error and uncertainty quantification and sensitivity analysis in mechanics computational models. *International Journal for Uncertainty Quantification* **2011,** *1* (2).

10. Hu, Z.; Mahadevan, S., Uncertainty quantification in prediction of material properties during additive manufacturing. *Scripta Materialia* **2017,** *135*, 135-140.

11. Frazier, W. E., Metal additive manufacturing: a review. *Journal of Materials Engineering and Performance* **2014,** *23* (6), 1917-1928.

12. Voinova, M.; Jonson, M.; Kasemo, B., 'Missing mass' effect in biosensor's QCM applications. *Biosensors and Bioelectronics* **2002,** *17* (10), 835-841.

13. Nguyen, N.-T.; Wu, Z., Micromixers—a review. *Journal of Micromechanics and Microengineering* **2004,** *15* (2), R1.

14. Dean, W.; Hurst, J., Note on the motion of fluid in a curved pipe. *Mathematika* **1959,** *6* (1), 77-85.

15. Gelber, M. K.; Kole, M. R.; Kim, N.; Aluru, N. R.; Bhargava, R., Quantitative Chemical Imaging of Nonplanar Microfluidics. *Analytical chemistry* **2017,** *89* (3), 1716-1723.

16. Stroock, A. D.; Dertinger, S. K.; Ajdari, A.; Mezić, I.; Stone, H. A.; Whitesides, G. M., Chaotic mixer for microchannels. *Science* **2002,** *295* (5555), 647-651.

Chapter 2

Soft mass measurement using MEM resonators

2.1 Introduction

MEMS-based resonant sensors have been extensively utilized as biological, physical and chemical sensors[1] for many years due to several advantages: 1) its simple geometry (e.g. cantilever beam structure), 2) possibility of using batch-fabrication, 3) proper for extreme miniaturization, even in the nanoscale, 4) high mass sensitivity. Because the resonant frequency of the sensor, w_0, is inversely proportional to the square root of its total mass ($w_0 \sim (1/m)^{0.5}$), measurement of resonant frequency shift between the system with and without the target mass gives the mass of target entity. Using this unique characteristics of the MEMS-based resonator, various physical quantities, such as the mass, stiffness, viscosity, and so on, have been measured: one of the commonly measured entities is the biological cells.[2]

The characterization of physical properties of cells such as their mass and stiffness has been gaining great interest and can have profound implications in cell biology, tissue engineering, cancer, and disease research.[3] Measurement of physical properties of cells enables the opportunity to unravel the questions that have not been answered in the evolution of biological systems. For example, the direct dependence of cell growth rate on cell mass for individual adherent human cells can elucidate the mechanisms underlying cell cycle progression.[4] There exist multiple ways to measure the mass and stiffness of the individual cell, and one of the widely-used devices to measure these quantities is MEM-based resonator.

In the previous studies, the resonant sensors that have cantilever geometry are used to measure the mass of various cells (e.g. HeLa cells).[5] However, it is commonly known that the

cantilever-type resonator has the non-uniform mass sensitivity that significantly changes based on the locations where the target is attached: the mass sensitivity is at its maximum when the added mass is placed at the free end of the cantilever and the sensitivity decreases to zero as the added mass gets to the fixed end of the cantilever. In other words, the measured mass reading is a function of the location of the cell relative to the free end determines the mass that is measured.[5] Figure 2.1 (a) shows the mass sensitivity of cantilever-type resonators with the color bar. It can be noticed that only the limited region near the tip of the cantilever has the mass sensitivity over 0.9.

Sometimes, the change in the cell mass is much smaller than the spatial variation of mass sensitivity in the resonator, the mass reading is not sufficient for elucidating the details of cell growth. The effect from the severe non-uniform mass sensitivity of the cantilever sensors can be reduced when a large number of the target entities are considered.[6] If this is the case, one can assume a uniform mass distribution over the resonator and uses an average mass sensitivity, which can be easily obtained with an analytical solution. However, if only a few or a single target entity is to be attached to the sensor, one cannot assume the uniform distribution of the target mass. One requires to adjust the extracted mass with the mass distribution from optical images of cantilevers,[7] or limit the attachment site to the end of the cantilever. These approaches reduce the actual mass sensitivity and make the mass sensor less practical to use.

In order to circumvent this limitation, a novel design of MEMS resonant mass sensor has been proposed, which has spatially uniform mass sensitivity on the pedestal (Figure 2.1 (a)).[8] This can be achieved by using the carefully designed half-folded springs that converts the flexural bending on the spring into the torsional bending at the folded point of the spring. The half-folded springs minimize the variation of the vibration amplitude across the vibrating platform, so that it achieves the uniform mass sensitivity. This sensor exhibits maximum 4%

differences of mass sensitivity on any position on the pedestal.[1b] Figure 2.1 (a) shows the mass sensitivity of the proposed resonator. On top of the pedestal, the mass sensitivity is quite uniform and all points have more than 0.96 mass sensitivity. The sensor operates in a first resonance mode, where the platform vibrates vertically at ~160 kHz in air and ~60 kHz in liquid.

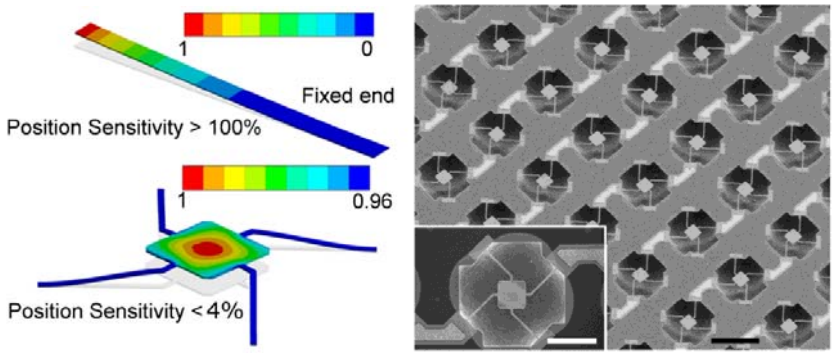

Figure 2.1 (a) The first mode of resonance is shown with the mass sensitivity (color bar) normalized to its maximum value. Modal analysis of cantilevers in liquid via finite element simulations shown that they have a spatially non-uniform mass sensitivity of greater than 100% from the free end of the cantilever to the middle of cantilever, whereas resonating platform designs demonstrate spatial non-uniformity of mass sensitivity to be less than 4% from the center to the edge of the platform. (b) SEM image showing sensor array, an individual sensor is shown in the inset.[9]

However, recent report has been shown that quartz crystal microbalance sensors produce a reduced mass reading of visco-elastic materials and the mass reading is increased as the stiffness of attached mass increases.[10] The reduced mass reading is called 'apparent mass', and this phenomenon is called 'missing mass effect'. Since the stiffness of the attached mass has a considerably lower than the sensor structure, the vibration phase of both deviates

significantly, resulting the effect of the inertial loading reduced. Therefore, it is necessary to measure the amount of coupling between stiffness of attached mass with reduced mass reading. In addition to the effect from the target's finite stiffness, there exists a chance that widely varying shape of the target entity affects the mass reading. Lastly, the device is often submerged into fluid to maintain the life of attached cells. This enhances the difficulty of estimating the true mass of the attached target as the mass reading from the device is the result of several different physical phenomena.

In this study, the finite element analysis is performed to investigate the effect of target's finite stiffness and its geometry on the apparent mass measurement. First, the parameters of simulation are carefully chosen to have the consistent resonant frequency measured by the experiment. Then, the target mass is modeled as an attached sphere on the resonator to simulate the behavior of the target mass during the measurement. The shape and mechanical property of the target mass is acquired from the experiment. Using the resonator and the target mass set-up, the effect of target's stiffness and its geometry on the mass reading is carefully studied.

2.2 Materials and methods

2.2.1 Finite element analysis

Finite element analysis was performed (ANSYS 12, ANSYS Inc., Canonsburg, Pennsylvania, USA), to investigate the effect of cell's finite stiffness and cell geometry on the apparent mass measurement as well as the interaction of the elastic silicon structure with the fluid medium. For modeling the dynamics of the submerged structure, the structural dynamics equation needs to be considered along with the fluid mass and momentum conservation equation. The mass and momentum conservation equations for inviscid fluid are:

$$\begin{aligned} &\frac{\partial \rho}{\partial t} + \nabla \cdot (\rho \vec{u}) = 0 \\ &\rho\left(\frac{\partial \vec{u}}{\partial t} + (\vec{u} \cdot \nabla)\vec{u}\right) = -\nabla p + \rho \vec{g} \end{aligned} \tag{2.1}$$

where ρ is the density, p is the pressure, g is the gravity, $\vec{u}$ is the velocity field in the fluid. The vibrating submerged structure produces fluctuations in pressure and density that propagates through the fluid.[] If the fluid is homogeneous, initially stationary and undergoes only small amplitude motion, those fluctuations can be expressed as:

$$\rho = \rho_0 + \rho', p = p_0 + p', \rho' << \rho_0, p' << p_0, |\vec{u}| << \mathrm{c} \sim \sqrt{\frac{p_o}{\rho_0}} \tag{2.2}$$

where the terms with subscript 0 stand for the initial state and the terms with primes means the fluctuation. The fluctuations are assumed to be a finite deviation from the initially uniform state (ρ_0, p_0) when the fluid is at rest $(\vec{u}_0 = 0)$. In this case, the mass and momentum balance equations can be written as the following equation.

$$\nabla^2 p' = \frac{1}{c^2}\frac{\partial^2 p'}{\partial t^2} \tag{2.3}$$

where c is the speed of sound inside the fluid.

In ANSYS software, the pressure formulated fluid element is used to model transient or harmonic state of the coupled fluid-solid system. This assumption is based on the facts that the amplitude of the resonator is small (~ 1.2 nm) compared with the dimension of the device and the fluid is inviscid. The finite element model of the fluid domain in the matrix form is

$$Q\ddot{p}' + C\dot{p}' + \mathrm{H}\, p' = f_2 + \rho_0 A^T \ddot{w} \tag{2.4}$$

where Q, C, H are the mass, damping, and stiffness matrices in fluid, respectively. f_2 is the external force and $A^T \ddot{w}$ is the interaction term from the structural part. If the structure is a rigidly mounted, homogeneous, isotropic, linear elastic material, the body moving in the transverse direction can be modeled as

$$M\ddot{w} + B\dot{w} + Kw = f_1 - Ap' \tag{2.5}$$

where w is the displacement in the structural part and M, B, K are the mass, damping, and stiffness matrices in solid, respectively. f_1 is the external force and Ap' is the interaction term from the fluid part. The governing equations for the fluid and solid elements take into account the coupling of the pressure and structural motion at the interface. The coupled equation for fluid structure interaction in this problem is as follows.

$$\begin{bmatrix} M & 0 \\ -\rho_0 A^T & Q \end{bmatrix} \begin{Bmatrix} \ddot{w} \\ \ddot{p}' \end{Bmatrix} + \begin{bmatrix} B & 0 \\ 0 & C \end{bmatrix} \begin{Bmatrix} \dot{w} \\ \dot{p}' \end{Bmatrix} + \begin{bmatrix} K & A \\ 0 & H \end{bmatrix} \begin{Bmatrix} w \\ p' \end{Bmatrix} = \begin{Bmatrix} f_1 \\ f_2 \end{Bmatrix} \tag{2.6}$$

2.2.2 Geometry of resonator and the target mass

The resonator consists of a square pedestal (60 x 60 μm) suspended by four beam springs (l = 80 μm, w = 4 μm) as shown in Figure 2.2. The edge of pedestal are chamfered around the size ~ 2 μm and the thickness of a silicon device layer is ~ 2 μm. The pedestal oscillates in the vertical direction while vibrating, and the end of four beam spring are fixed to the substrate.

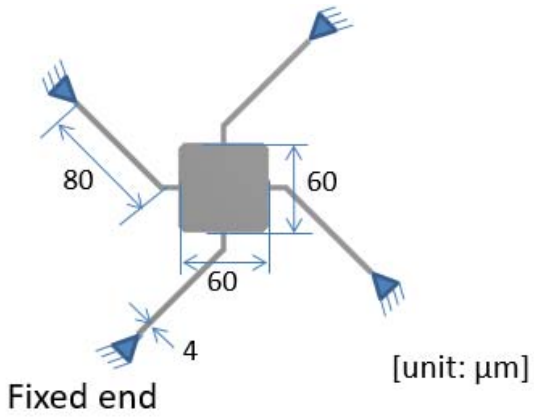

Figure 2.2 Geometry of the resonator with dimensions.

2.2.3 Geometry of target mass

The shape of target mass is a simplified as a sphere which is partially attached to the device. The volume and cross sectional area are estimated by image analysis from confocal and dark field microscopy images. Figure 2.3 shows the cell volume and the cross-sectional area that are obtained from the experiments (blue and red) and fitting curve (green) that is used for the modeling the target mass.

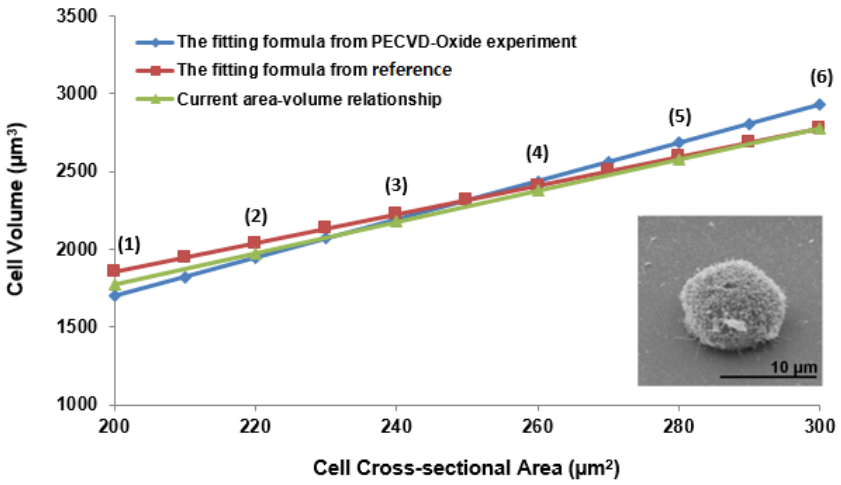

Figure 2.3 The shape of target mass is modeled as a sphere that is partially attached to the device based on the experimental data. 6 different shapes and volumes are selected to study the effect of the geometry of the target mass.

2.3 Results and discussions

2.3.1 Resonant frequency matching

The resonant frequencies obtained with the 3D finite element analysis are 170±48 kHz in air and 59.6±3.2 kHz in liquid. Through the sensitivity analysis of multiple parameters in the experiment, there exist three parameters that affect dominantly on the resonant frequency of the resonator: Young's modulus and thickness of the resonator, and fluid density. Each parameter is carefully calibrated in order to match the resonant frequency of the device between the simulation and the experiment.

First, the effect of Young's modulus on the resonant frequency of the resonator is studied. The Young's modulus of silicon varies in different directions in the material relative to the crystal orientation. (100) wafers are the most common one, but as we do not have the prior information regarding the orientation, the uniform possibility over the certain range is assumed. The Young's modulus is 169 GPa and 130 GPa for the direction parallel to flat and 45° diagonal to flat, respectively. This range of Young's modulus changes the resonant frequency of the resonator 170±13 kHz.

Second, there exist a certain uncertainty in measurement of resonator's thickness. The possible range of thickness of the resonator is 2.0±0.5 μm, considering the measurement error. The non-uniformity of the device thickness is not considered in this study. The resonant frequency of the resonator decreases as the thickness increases within this range. The deviation in the device thickness, 2.0±0.5 μm, changes the resonant frequency, 170±42 kHz.

The careful optimization procedure is employed to find the proper values for the Young's modulus and the thickness of the resonator, resulting 150 GPa and 1.88 μm, respectively. By using these values, the resonant frequency of the device is 148.32 kHz, which has a good agreement with the resonant frequency of the device in air.

For the last step, the effect of the density of surrounding fluid is analyzed, so that we can confirm the resonant frequency of the device is well matched with the experiment and proceed to study the effect of attached mass on top of the device. The resonator is submerged in the cell growth medium (L-15 media with 30 % Fetal Bovine Serum (FBS)). According to L-15 formulation, 13.8 g of L-15 powder is added to a liter of medium. Based on the formula and the relative densities of FBS as well as the water, we can calculate the density of growth medium. The possible density deviations due to the error in the specific density of FBS takes into consideration. Therefore, the range of density of fluid is 998±50 kg/m^3. By changing the fluid density within range ± 5 % and ± 10 %, the resonant frequency of the device in the growth medium is changed around 3 % and 6 %, respectively. The result after the careful optimization procedure is shown in Table 2.1.

Table 2.1 The resonant frequency of the device in the experiment and the simulation.

	Experiment (kHz)	**Simulation (kHz)**
In air	170±48	148.32
In fluid	59.6±3.2	57.62

2.3.2 Effect from the position of target mass on mass measurement

To explain the effect of the target position on the mass measurement, 3D finite element analysis was performed with ANSYS software. The position of target mass is located from the center of the pedestal and changed to other locations. The exact locations as well as the given mass, the measured mass from the frequency shift is given in Figure 2.4 and Table 2.2. The results show that the position of the target mass on the mass reading affects less than 4% of its actual mass when it's almost at the edge of the pedestal. This is consistent with the mass sensitivity that we have previously.

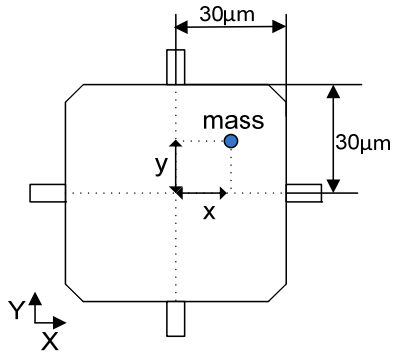

Figure 2.4 The position effect on the apparent mass is studied by changing the location of target mass on the pedestal. The target mass is modeled as a point and the stiffness is infinite to remove the effect from the finite stiffness of the target. The specific locations of the target mass is given in Table 2.2.

Table 2.2 The position effect on the apparent mass.

Target mass location (x μm, y μm)	Apparent mass for 1.0 ng target mass	Apparent mass for 2.0 ng target mass
(0,0)	1.012	2.012
(5,5)	1.016	2.015
(10,10)	1.016	2.027
(15,15)	1.024	2.027
(20,20)	1.031	2.035
(25,25)	1.039	2.039

2.3.3. Effect of Young's modulus on mass measurement

The effect of Young's modulus of the target mass on the mass reading is studied. The 6 different shapes that are extracted from the experiment are used to check the obtained trend is consistent even if the shape of the target mass is changed. Figure 2.5 shows the effect of target's Young's modulus on the mass reading. X-axis is the Young's modulus of the target changing from 5 kPa to 500 kPa. These values are chosen from the reference, considering the

stiffness of the cell. Y-axis is the apparent mass that is calculated from the frequency shift in the simulation. As the Young's modulus increase the apparent mass converges to its true mass within ± 2 % deviation. The simulation results confirm that above the certain Young's modulus of the target, the mass reading of the resonant sensor is within the error bound. Additionally, this is true even if the geometry of the target is changed.

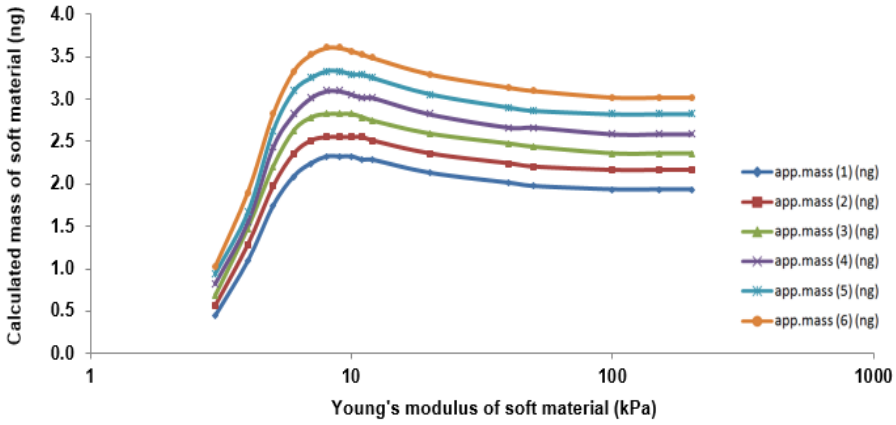

Figure 2.5 The target's Young's modulus effect on the apparent mass is studied. The Young's modulus is changed from 5 kPa to 500 kPa based on the experimental data. Above the certain Young's modulus value (100 kPa), the apparent mass is within ± 2 % deviation bound from the true target mass.

2.3.4. Effect from the geometry of target on mass measurement

To explain the effect of the cell geometry on the mass measurement, 3D finite element analysis was performed with ANSYS software. The cell on sensor was modeled as a sphere made with the elastic material that was attached to the platform. The structural damping coefficient was chosen as ~0.45. The system including the device and the cell was submerged in the fluid. We assume that the cell is attached tightly in the vertical direction and the Coulomb friction model is used in the tangential direction. Harmonic analysis is performed to determine

the steady-state response of the system to cyclic loads over a frequency range. Due to the characteristics of harmonic analysis in ANSYS, all the nonlinearities are linearized, based on its initial state. The four legs of the device are fixed and a harmonic force was given on the platform to generate the same vibration amplitude on the platform. Based on the harmonic response of the system with a step size ~10Hz, the resonant frequency is determined. The apparent mass was calculated from the spring constant, the resonant frequency of the sensor with and without the cell.

In order to model different geometries of the cell on the platform (Figure 2.6 (a)), we change the cell height and the contact area between the cell and the platform, while the volume and the density of the cell are conserved. The cell volume and the cross sectional area are measured in the experiment. The Young's modulus of the cell was chosen as 5 kPa for a live cell and as 50 kPa for a fixed cell, based on the experimental data and model extraction. To clarify the relationship between the contact area and the apparent mass of the cell, the apparent mass was normalized with respect to the actual cell mass. Figure 2.6 (b) shows that the apparent mass sharply decreases as the cell contact area is smaller than 200 μm^2.

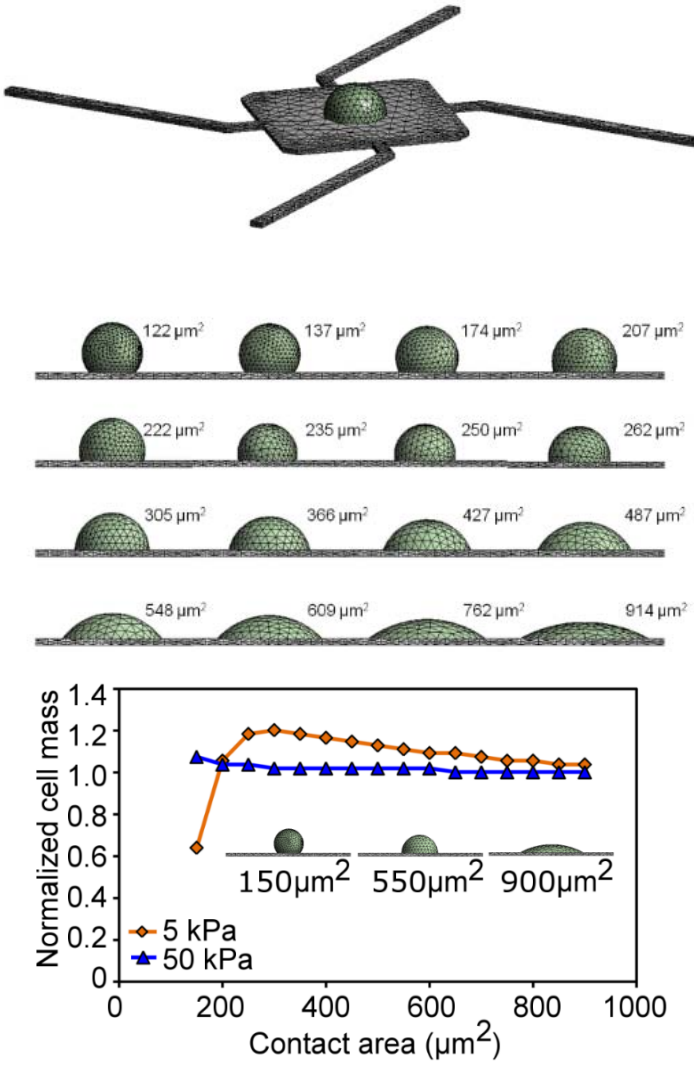

Figure 2.6 (a) 16 different attached mass geometry while the volume is maintained. (b) The effect of the cell geometry to the mass measurement of the cell with a constant volume.[9]

The variation of the mass reading ratio with Young's modulus of the cell is plotted in Figure 2.7. To compute the effect of Young's modulus on the mass reading ratio, the Young's modulus of the cell is changed while the geometry including its volume is kept the same. Due to the inherent characteristics of the cell, the mass reading from the platform is lower than the actual mass in the case of small Young's modulus. As the Young's modulus increases, the mass reading ratio converges to 1, which means that the apparent mass converges to the actual

mass. The error bars are due to the results from the six different cell geometries. All the cell geometries are based on the experiments.

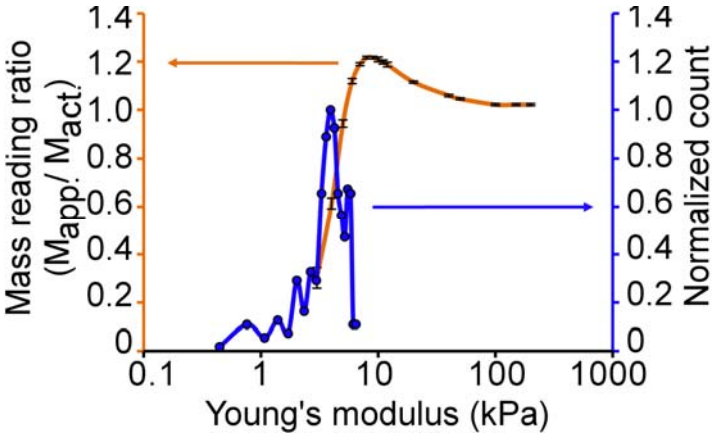

Figure 2.7 Calculated dependence of the reading ratio on the stiffness of the cell is shown in orange curve and the normalized histogram of the Young's modulus is shown in blue curve.[9]

2.4 Conclusion

In this work, we were able to account for the effects of shape and stiffness of the cell on the measurement of cell mass using the finite element model. Our results indicate that the apparent cell mass measured by the proposed resonator could depend on the stiffness of the cell. Such a model can also be used to explain the previously observed "missing mass effect." It should be noted that the finite element model in the analysis is a simplified one, and while it can elegantly capture the essential mechanisms, it should only be expected to yield a trend rather than accurate quantitative results. Considering the elasticity and viscosity of the cell improves the understanding of the cell mass measurement in the experiment, which is limited in the existing simulation methods that treat the cell as a point mass perfectly attached to the sensor.

In conclusion, the simulation expands our understanding about the effect of shape and stiffness on the mass measurement using the resonator. Moreover, it can explain the reduction of mass reading of resonator, called "missing mass effect." We believe that our system can make a significant contribution to understanding the behavior of soft mass on top of resonator.

2.5 References

1. (a) Waggoner, P. S.; Craighead, H. G., Micro-and nanomechanical sensors for environmental, chemical, and biological detection. *Lab on a Chip* **2007,** *7* (10), 1238-1255; (b) Park, K.; Jang, J.; Irimia, D.; Sturgis, J.; Lee, J.; Robinson, J. P.; Toner, M.; Bashir, R., 'Living cantilever arrays' for characterization of mass of single live cells in fluids. *Lab on a Chip* **2008,** *8* (7), 1034-1041.

2. Godin, M.; Bryan, A. K.; Burg, T. P.; Babcock, K.; Manalis, S. R., Measuring the mass, density, and size of particles and cells using a suspended microchannel resonator. *Applied Physics Letters* **2007,** *91* (12), 123121.

3. Brownlee, M., Biochemistry and molecular cell biology of diabetic complications. *Nature* **2001,** *414* (6865), 813-820.

4. Mir, M.; Wang, Z.; Shen, Z.; Bednarz, M.; Bashir, R.; Golding, I.; Prasanth, S. G.; Popescu, G., Optical measurement of cycle-dependent cell growth. *Proceedings of the National Academy of Sciences* **2011,** *108* (32), 13124-13129.

5. Dohn, S.; Sandberg, R.; Svendsen, W.; Boisen, A., Enhanced functionality of cantilever based mass sensors using higher modes. *Applied Physics Letters* **2005,** *86* (23), -.

6. Thundat, T.; Wachter, E.; Sharp, S.; Warmack, R., Detection of mercury vapor using resonating microcantilevers. *Applied Physics Letters* **1995,** *66* (13), 1695-1697.

7. Ilic, B.; Czaplewski, D.; Zalalutdinov, M.; Craighead, H.; Neuzil, P.; Campagnolo, C.; Batt, C., Single cell detection with micromechanical oscillators. *Journal of Vacuum Science & Technology B: Microelectronics and Nanometer Structures Processing, Measurement, and Phenomena* **2001,** *19* (6), 2825-2828.

8. Park, K.; Bashir, R. In *MEMS-based resonant sensor with uniform mass sensitivity*, TRANSDUCERS 2009-2009 International Solid-State Sensors, Actuators and Microsystems Conference, IEEE: 2009; pp 1956-1958.

9. Park, K.; Millet, L. J.; Kim, N.; Li, H.; Jin, X.; Popescu, G.; Aluru, N.; Hsia, K. J.; Bashir, R., Measurement of adherent cell mass and growth. *Proceedings of the National Academy of Sciences* **2010,** *107* (48), 20691-20696.

10. Voinova, M.; Jonson, M.; Kasemo, B., 'Missing mass' effect in biosensor's QCM applications. *Biosensors and Bioelectronics* **2002,** *17* (10), 835-841.

Chapter 3

Helical micromixer from sacrificial 3D printing

3.1 Introduction

Precise control of small quantities of fluids in microfluidic devices makes it widely used to observation of various systems, including chemical, biological and physical systems.[1] The shape of most microfluidic devices are limited to have rectangular cross-sections since the current state of fabrication method involves lamination of planar structure. Although the majority of the current microfluidic channels have the rectangular shape, most of biological flow channels have circular cross-sections. This changes the characteristics of fluid flow inside the channel, which cannot be captured in devices with rectangular cross-sections.[2]

There exists several techniques to fabricate round microchannels, including bonding of open semicircular channels, viscous finger pattering in rectangular channels, and monolithic sacrificial molding. The bonding approach uses milling and molding processes to create two semicircular open channels.[3] By aligning and bonding, the two halves of the chip yield a planar network of channels. In the viscous fingering approach, the rounded cross-sections are generated by the surface tension modulation of the multiphase flow in rectangular cross-section channel. Even though these approaches are useful in various areas,[2b, 4] it cannot be used to make a channels in general shapes, such as split and recombined shapes. In the monolithic casting approach, the polymer before the curing process is casted around the template shape in the desired channel, and the template is remove in order to have a channel with desired shape. The wide options for the material for the template are available, such as a polymer thread,[5] a glass fiber,[6] or a wire.[7] This method produces a monolithic chips with

circular cross-sectional channel, but assembling a sacrificial model from pre-formed filament into the desired channel geometry is challenging.

Direct-writing technique solves this problem by generating the sacrificial material through a cylindrical nozzle into a supporting liquid or colloidal reservoir[8] or, in free space if the material can be stiffened rapidly. This method is called "freeform" 3D printing. The materials that is rapidly stiffened can be used: UV curing,[9] solvent evaporation,[10] or natural cooling.[11] Sugars and sugar alcohols are also widely used in the freeform printing for the complex geometries due to its advantages: biocompatible, solubility in water, etc.[12] However, it has not been shown that channel networks fabricated in the freeform way can be applied to the classical mixing problem. In addition, the mixing behavior inside the channels has not been validated or discussed due to the limitation of imaging flow inside the channels.

In the microfluidic devices, one of the major necessities in the device is mixing multiple fluids.[13] There exists two ways to mix fluids: active and passive mixers. The active mixers utilize the energies in various sources, such as electrical, acoustic, or thermal, to enhance the mixing rate. On the other hand, the passive mixers use the geometrical features in the channel. Due to its simplicity of device set-up and low energy consumption, the passive mixers have been drawn much attention, and numerous designs for the effective passive mixer have been proposed for many years. One of the widely used design is the staggered herringbone mixer.[14] This device uses its unique herringbone pattern to induce the local chaotic motion, which significantly increases the mixing rate. However, a large number of design parameters as well as complex manufacturing processes make the herringbone mixer less practical.

Therefore, we focus on the mixing mechanism that uses the Dean effect. The formation of symmetric vortices and the role of centrifugal forces was first presented by Dean in 1927 and 1928.[15] A fluid flow around a curved path generates the centrifugal acceleration of fluid,

resulting a secondary transverse flow. This transverse flow causes the interface between two fluids to fold, which enhances the interfacial area and diffusive transport.[16] The major challenge is maintaining the folded interface over a sufficient distance, so that the diffusive transport occur. The comparative effects of centrifugal force to viscous force are characterized and explained by the Dean number as follows:

$$De = \mathrm{Re}\sqrt{\frac{r}{R}} = \frac{2Q}{v\pi}\sqrt{\frac{1}{rR}} \tag{3.1}$$

where Re is the Reynolds number, Q is the mass flow rate, v is the kinematic viscosity, r is the radius of the channel cross-section, and R is the radius of curvature. As De increases, the effect from the transverse flow grows. In a planar device, a spiral shape of mixer are widely used to maximize De. In a 3D device, the helical shape are preferred because it maintains high De for an arbitrary number of turns without changing R and r.

Considerable investigations have been performed to understand the effect of secondary flows in curved channels, enhanced shear stresses, and heat transfer.[17] Though the flow of a homogeneous fluid in a helical channel has been described analytically,[18] mixing of two different fluids in a helical channel has not been explained fully because it requires to understand the spatial variation in fluid density and viscosity and the diffusion of dissolved species. Recent advancement in computing power as well as numerical modeling techniques enable the accurate numerical simulation of this mixing behavior, and others have investigated the mixing efficiency in spirals[19] and helices.[20] However, none of the previous studies has been shown the complete comparison of the mixing behavior of two distinctive fluids inside the helical mixer between the experiment and the numerical prediction.

Here we simulate the complete mixing behavior of two fluids inside the 3D helical mixer with a round-channel. In order to compare this computational result with the experiment, we use a freeform 3D printed sacrificial template to fabricate a round-channel helical mixer. The refractive index of a polymer that is used in making channels are carefully chosen to visualize the mixing behavior inside the 3D helical mixer. The stimulated Raman scattering (SRS) microscopy is used to measure the concentration of any Raman-active molecule at all points inside the channel. 3D chemical images of the mixing of glucose and saltwater are acquired through SRS microscopy. The measured concentration in the simulation and mixing performance in the experiment closely agree with each other. The mixing performance of the helical mixer is compared with the staggered herringbone mixer. Based on the results we calculate, the helical mixer outperforms over the optimized herringbone mixer in terms of pressure drop, mixing volume, and mixing time above a critical Reynolds number. This results show the possibility of using the helical mixer as a novel mixing device in various applications. In addition, it demonstrate the possibility of optical imaging as well as the broad utility of SRS imaging for directly quantifying chemical concentration fields in 3D microfluidic devices.

3.2 Materials and methods

3.2.1 Modeling

The mixing behavior of the glucose and saltwater was modeled using the COMSOL Multiphysics Package (COMSOL Group, Stockholm, Sweden). The geometry of the model, including major and minor diameters, pitch distance, and the number of turns, were matched to the experimental set-up. The simulation solved the steady state, incompressible Navier-Stokes (NS) equation for conservation of mass and momentum without the external force field:

$$\begin{aligned} &\nabla \cdot u = 0 \\ &\rho(u \cdot \nabla)u = \nabla \cdot [-pI + \mu(\nabla u + (\nabla u)^T)] \end{aligned} \tag{3.2}$$

where $_u$ is the velocity, p is the pressure, ρ is the density, and μ is the viscosity of the fluid. The use of continuum mechanics is justified by calculation of the Knudsen number as less than 0.01.[21] In addition, the coupled convection-diffusion (CD) equation of a diluted species was used to model the transport of glucose and saltwater, tracking the location of the interface between two solutions:

$$\nabla \cdot (D\nabla c) + u \cdot \nabla c = 0 \tag{3.3}$$

where $_c$ represents the relative concentration of the sodium and glucose solutions. The converged solution of NS was fed into CD with the velocity field, and the CD equation coupled back with the NS equation through the dependence of the density and viscosity on the relative concentration. We approximated the mixed fluid viscosity and density as a linear interpolation function between two solutions:

$$\mu = c\mu_1 + (1-c)\mu_2$$
$$\rho = c\rho_1 + (1-c)\rho_2 \quad (3.4)$$

where the indices 1 and 2 stand for the sodium and glucose solutions, respectively. Values for viscosity, density, and the diffusion coefficient of 8 wt % glucose and 5.7% wt saltwater were taken from the literature.[22] We assumed that the mutual interaction between two solutions on diffusion coefficient is small enough not to affect the whole mixing behavior. The no-slip boundary condition on the walls was applied, as is appropriate for microchannels of hydraulic diameter greater than 30 μm.[23]

We used several techniques to reduce the complexity of computational fluid modelling with μ-level resolution accuracy: 1) The NS and the CD equations were calculated separately to reduce the computational cost. 2) The computational domain in NS and CD equations was divided into two parts. For the first part of the domain, the inlet velocity and concentration profiles were specified, matching the experimental set-up, and the passive outlet boundary condition (p=0 for NS, or convective flux condition for CD) was applied. The velocity and concentration profiles at the outlet were exported, and imported as an inlet conditions for the second part of the domain to complete the results. 3) To improve the convergence of the simulation, the initial conditions of the high inlet volume flow rate cases were set through viscosity ramping, starting from higher viscosities (weakly nonlinear problem), and progressively increasing the nonlinearity until the original problem (highly nonlinear problem) is solved.

Modeling of the herringbone mixer was performed using the optimized design given in the reference[24] with W = 380 μm, d/h = 0.48, and θ = 53.2. The mixing time *T*, pressure drop *P*, and mixing volume *V*, were then determined for a mixer in which W = 480 μm using the following relations:

$$\frac{T_2}{T_1} = \left(\frac{W_2}{W_1}\right)^2$$
$$\frac{P_2}{P_1} = \left(\frac{W_1}{W_2}\right)^2 \qquad (3.5)$$
$$\frac{V_2}{V_1} = \left(\frac{W_2}{W_1}\right)^2$$

These scaling relations are derived from the assumption that the mixing profile is purely a function of the Péclet number. W_2/W_1 =1.26 was chosen so that the *P* and *V* curves for the helical mixer crossed the corresponding curves for the herringbone mixer at the same value of *Re*.

3.2.2 Image processing

All spectroscopic images taken by SRS imaging microscope are processes in Matlab (The Mathworks, Nantucket, MA) in order to compare the experimental results with the simulation results. The simulation meshes were mapped onto a square grid of effective pixel size 2 μm. Additionally, the noise component that exists in the SRS images are taken into consideration when extracting performance metrics from the experimental data. The relative unmixing index *I* is given by the following expression:

$$I = \sqrt{\frac{\frac{1}{N}\sum_{j=1}^{N}(x_j - \bar{x}_j)^2}{\frac{1}{N}\sum_{i=1}^{N}(x_i - \bar{x}_i)^2}} \qquad (3.6)$$

where x_i are the pixel intensities at the inlet and x_j the pixel intensities at the cross section of interest. *N* is the total number of pixels. The correction term for the noise in the experimental

images are taken into consideration. The variance noise intensities, σ_n^2, is subtracted from the total variance at each cross section:

$$I = \sqrt{\frac{\frac{1}{N}\sum_{j=1}^{N}(x_j - \bar{x}_j)^2 - \sigma_n^2}{\frac{1}{N}\sum_{i=1}^{N}(x_i - \bar{x}_i)^2 - \sigma_n^2}} \tag{3.7}$$

3.3 Results and discussions

3.3.1 Mixer geometry

The helical mixer with circular cross-section is made by using the sacrificial template process. The outer diameter of the helix is 780 μm and the diameter of the circular channel is 155 +/-3.5 μm. Based on these values, the calculated major diameter of the helix is 625 μm, which is 7.4% smaller than the programmed diameter. The reduction of diameter is due to the constant radial acceleration of the nozzle, which pulls the filament that is still molten. The same phenomenon is observed in other approaches to freeform printed helices.[25] The total number of turns is 8.5 and the pitch of the helix is 500 μm.

3.3.2 Mixing performance

The mixing performance of the helical mixer is evaluated in every ½ helix turn inside the channel. Visualizing cross-sections every ½ helix turn is readily accomplished by focusing the microscope objective to the center of the mixer and acquiring a single image along the entire length of the device. By adjusting the scale of the image such that 'pure' saltwater (5.7% by weight) at the mixer inlet has a value of 0 and 'pure' glucose solution (8% by weight) at the mixer inlet has a value of 1, the images are scaled to match glucose concentration. In the simulation, the concentration map of two fluids at the corresponding cross sections are extracted from the entire data set. Similarly, the relative concentration values at each mesh show the concentration of glucose and saltwater. This value changes from 0, meaning pure glucose solution, to 1, meaning the pure saltwater.

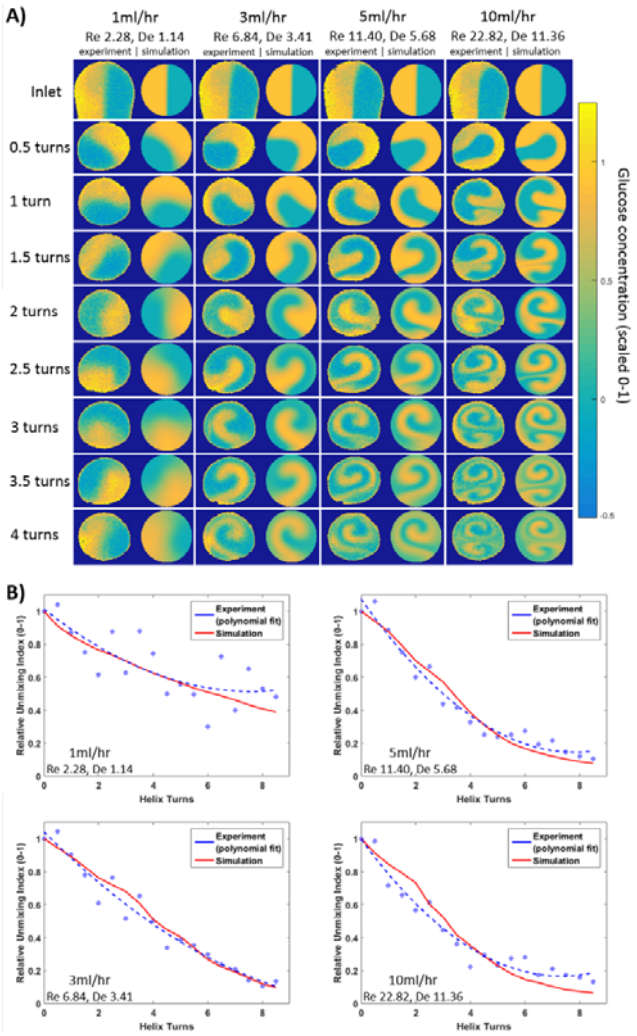

Figure 3.1 (a) Experimental and simulation (COMSOL) visualization of glucose concentration at several cross sections in the helical mixer for four different flow rates from 1 ml/hr to 10 ml/hr (Raynold's and Dean's numbers also shown). The SRS images have been scaled to show absolute glucose concentration from 0-1, although pixels outside of this range appear due to noise. (b) Relative unmixing index as calculated from these cross section images for experiment and simulation by comparing the standard deviation of the 'inlet' condition to each other cross section. The noise in the SRS images (RMS power 0.125 on a scale of 1) was taken into account for these calculations. A second-order polynomial fit is provided to guide the trend for the experimental data points, but is not meant to imply the underlying behavior of the system.[26]

Figure 3.1 shows the glucose concentration at several channel cross-sections as measured by SRS imaging and as predicted by numerical modeling. As expected for a laminar regime with a very controlled geometry, the agreement is excellent. Furthermore, the only experimental parameters used to generate the model were the optically measured major and minor radii, R and r, and the density and viscosity properties of saltwater and glucose solutions as obtained from the literature. The simulated geometry was thus a perfectly helical pipe, and the inlet boundary condition was a symmetric distribution of the two input fluids such that their interface was parallel to the helical axis. With the relatively small number of parameters with the well-controlled geometry of the device, the fidelity of the numerical simulation is confirmed, so that it can be used to modeling and optimization process prior to actual fabrication.

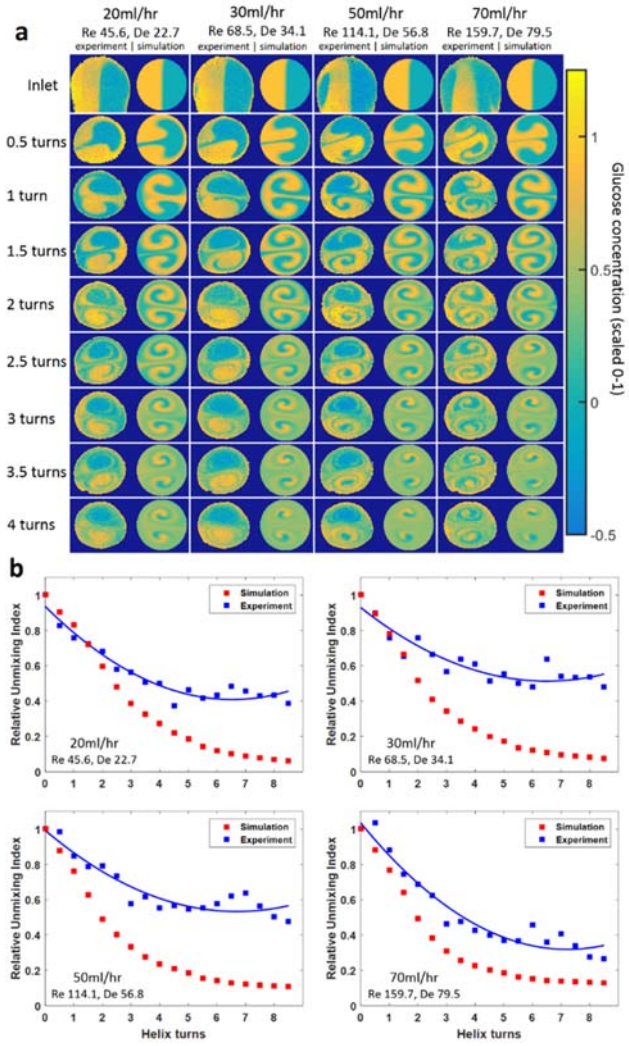

Figure 3.2 (a) Experimental and simulation (COMSOL) visualization of glucose concentration at several cross sections in the helical mixer for four different flow rates from 20 ml/hr to 70 ml/hr (Raynold's and Dean's numbers also shown). (b) Relative unmixing index as calculated from these cross-section images for experiment and simulation. Trendlines to the experiment are derived using the best fit for second order polynomials.[26]

For the experiments at higher *De* (Figure 3.2), there is deviation between the model and experiment due to an entrance effect that is not captured in the model's inlet boundary condition. Slight asymmetry in the T-junction where the inlet channels meet causes the interface of the 2 fluids to rotate slightly before it enters the helix. This slight asymmetry in

the junction accumulates as the fluid proceeds, so that the difference between the model and experiment becomes significant. At these higher values of *De*, the mixing performance becomes strongly dependent on the orientation of the fluid interface at the device inlet. Figure 3.3 demonstrates the effect of the inlet interface orientation on mixing. The inlet interface orientation changes from 0 ° to 90 °, and the corresponding mixing performance are compared to each other. When the interface orientation is 0 °, the mixing performance is maximized because the induced secondary transverse flow from Dean's effect is vertical to the interface orientation. However, when the secondary transverse flow is parallel to the interface orientation (90 °), there is no significant advantage in mixing performance from the Dean's effect. This is clearly explained by the relative unmixing index for each inlet condition along the length of the helix in Figure 3.3 (b).

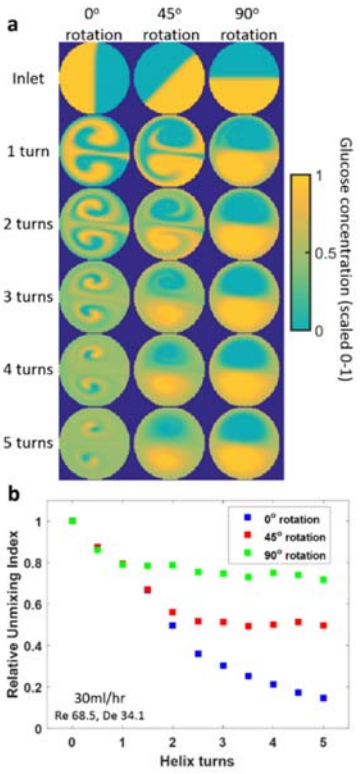

Figure 3.3 Effect of inlet rotation on mixing length. (a) COMSOL simulations of glucose concentration at cross sections in the helical mixer for three different inlet conditions at De = 34.1. (b) Relative unmixing index for each inlet condition along the length of the helix.[26]

3.3.3 Performance analysis

To compare the mixing performance of the helical mixer to an existing standard, we use the staggered herringbone mixer with optimized design parameters.[24] The geometry of the staggered herringbone structure is scaled to match the mixer volume and pressure drop at the same value of Re, so that the performance of both devices are compared in the same condition. The measure of performance is determined by the relative unmixing index, which uses the ratio of the standard deviation of the pixel intensities at a given cross section to the standard deviation at the inlet. The expression for the relative unmixing index is given in Equation (3.7). This value changes between 0 and 1, where 0 represents perfect mixing and 1 no mixing. The evolution of the unmixing index of the helical mixer at consecutive cross-sections is shown in Figure 3.1 and Figure 3.2. The unmixing index of the staggered herringbone mixer at corresponding cross-sections is obtained from the numerical model. The locations of corresponding cross-sections in the herringbone mixer means the locations which have the same fluid traveling distance with the helical mixer. Then, the mixer performance at each chosen cross-sections is quantified in terms of the amount of volume, time, and pressure head required to achieve a relative unmixing index of 0.15 (Figure 3.4).

The concentration profile in the mixing is a function of the Péclet number (Pe=Q/LD), which is the dimensionless number relevant to the relative importance between convective motion and diffusive motion. L is the characteristic length, and D is the diffusion coefficient. Thus, when the D is fixed, the same mixing profile will occur for constant values of Q/L. However, the mixing time, mixer volume and pressure drop scale as follows: $T \propto L^2$, $P \propto L^{-2}$, $V \propto L^3$. Since the dimensions of the herringbone mixer is scaled to match the mixer volume and pressure drop in both mixers at the same value of Re, this occurred at Re = 10. For the flow that has Re<10, the volume and pressure drop were lower for the herringbone mixer. This means the energy consumption in the herringbone mixer is lower than the helical mixer. On

the other hand, for Re<10, the volume and pressure drop is lower for the helical mixer, meaning the energy consumption is lower in the helical mixer. At all values of Re, the mixing time was lower for the helical mixer.

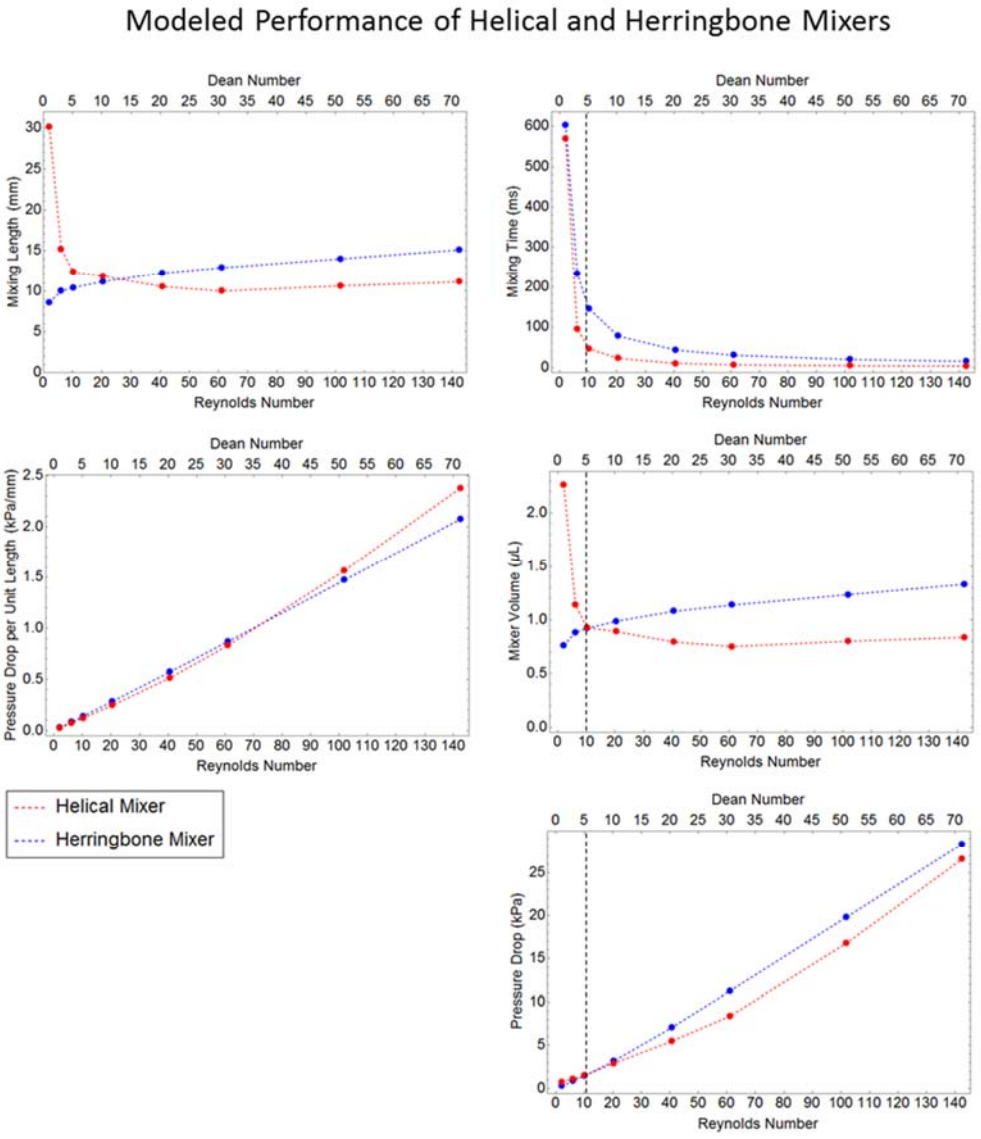

Figure 3.4 Comparison of helical and herringbone mixers. Data points for mixing length, time, volume, and pressure drop are each the minimum value required to obtain 85% mixing.

In this study, the systematic optimization process has not been performed, but there exists a rough guideline to qualitatively understand the optimized geometry of helical mixer. The performance of a mixer can be quantified in terms of the mixing time, the mixer volume, and the pressure drop across the mixer. The helical mixer performance is maximized when the curvature is maximized and torsion is minimized. This can be easily expected by checking the Dean's number. Therefore, optimizing the geometry of the helical mixer requires varying one geometric parameter, which is the channel radius. We expect the fact that the optimized geometry of helical mixer will show the better performance than the one presented in this report. In contrast, the geometry of the staggered herringbone mixer is defined by 6 parameters,[24] and optimization requires to explore a large parameter space.

The result shows, for Re>10, the helical mixer outperformed the herringbone mixer by all three metrics. The main reason for better performance is due to the circular cross-section in the helical mixer. Since the circular section minimizes the contact length between the fluid and the channel, it also minimizes the energy loss due to viscosity for a given volume. This also reduces the hydraulic pressure drop and increases the convective mass transport. This difference is significantly enhanced when there exist multiple hydraulic components are connected in series in the system. The sum of pressure drops may cause bonded chips to delaminate and soft PDMS chips to deform.[27] Even if monolithic devices are immune to be failed by delamination, the lower pressure drop of the system is always preferable because the lower pressure drop of a helical mixer at higher Re allows for high flow rates and placement of multiple components in series without risking deformation.

3.4 Conclusion

In this work, the mixing behavior of two fluids inside the helical mixer is analyzed. The computational model that can capture the details of mixing performance is developed and carefully selected parameters are used for the simulation. The simulation results are compared with the experimental results with the same geometry. The full 3D helical mixer is generated by using a novel fabrication procedure via sacrificial molding of freeform 3D printed isomalt. The measured mixing behavior of two fluids inside the helical mixer is compared with the numerical model to ensure the validity of the computational model. We investigate the effect of experimental parameters on mixing performance and demonstrate the effectiveness of the helical mixer by comparing the performance of the mixer with the herringbone mixer. The numerical model that is used in this study can be extended for analysis of the various mixers that have complex geometry.

3.5 References

1. Whitesides, G. M., The origins and the future of microfluidics. *Nature* **2006,** *442* (7101), 368-373.

2. (a) Lima, R.; Oliveira, M. S.; Ishikawa, T.; Kaji, H.; Tanaka, S.; Nishizawa, M.; Yamaguchi, T., Axisymmetric polydimethysiloxane microchannels for in vitro hemodynamic studies. *Biofabrication* **2009,** *1* (3), 035005; (b) Yang, X.; Forouzan, O.; Burns, J. M.; Shevkoplyas, S. S., Traffic of leukocytes in microfluidic channels with rectangular and rounded cross-sections. *Lab on a Chip* **2011,** *11* (19), 3231-3240.

3. (a) Jang, M.; Kwon, Y. J.; Lee, N. Y., Non-photolithographic plastic-mold-based fabrication of cylindrical and multi-tiered poly (dimethylsiloxane) microchannels for biomimetic lab-on-a-chip applications. *RSC Advances* **2015,** *5* (122), 100905-100911; (b) Borenstein, J. T.; Tupper, M. M.; Mack, P. J.; Weinberg, E. J.; Khalil, A. S.; Hsiao, J.; García-Cardeña, G., Functional endothelialized microvascular networks with circular cross-sections in a tissue culture substrate. *Biomedical microdevices* **2010,** *12* (1), 71-79; (c) De Ville, M.; Coquet, P.; Brunet, P.; Boukherroub, R., Simple and low-cost fabrication of PDMS microfluidic round channels by surface-wetting parameters optimization. *Microfluidics and nanofluidics* **2012,** *12* (6), 953-961; (d) Huang, Z.; Li, X.; Martins-Green, M.; Liu, Y., Microfabrication of cylindrical microfluidic channel networks for microvascular research. *Biomedical microdevices* **2012,** *14* (5), 873-883; (e) Choi, J. S.; Piao, Y.; Seo, T. S., Fabrication of a circular PDMS microchannel for constructing a three-dimensional endothelial cell layer. *Bioprocess and biosystems engineering* **2013,** *36* (12), 1871-1878; (f) Choi, J. S.; Piao, Y.; Seo, T. S., Circumferential alignment of vascular smooth muscle cells in a circular microfluidic channel. *Biomaterials* **2014,** *35* (1), 63-70; (g) Wilson, M. E.; Kota, N.; Kim, Y.; Wang, Y.; Stolz, D. B.; LeDuc, P. R.; Ozdoganlar, O. B., Fabrication of circular microfluidic channels by combining mechanical micromilling and soft lithography. *Lab on a Chip* **2011,** *11* (8), 1550-

1555.

4. (a) Fiddes, L. K.; Raz, N.; Srigunapalan, S.; Tumarkan, E.; Simmons, C. A.; Wheeler, A. R.; Kumacheva, E., A circular cross-section PDMS microfluidics system for replication of cardiovascular flow conditions. *Biomaterials* **2010,** *31* (13), 3459-3464; (b) Abdelgawad, M.; Wu, C.; Chien, W.-Y.; Geddie, W. R.; Jewett, M. A.; Sun, Y., A fast and simple method to fabricate circular microchannels in polydimethylsiloxane (PDMS). *Lab on a Chip* **2011,** *11* (3), 545-551; (c) Bischel, L. L.; Lee, S.-H.; Beebe, D. J., A practical method for patterning lumens through ECM hydrogels via viscous finger patterning. *Journal of laboratory automation* **2012,** *17* (2), 96-103.

5. (a) Verma, M. K.; Majumder, A.; Ghatak, A., Embedded template-assisted fabrication of complex microchannels in PDMS and design of a microfluidic adhesive. *Langmuir* **2006,** *22* (24), 10291-10295; (b) Hunziker, P. R.; Wolf, M. P.; Wang, X.; Zhang, B.; Marsch, S.; Salieb-Beugelaar, G. B., Construction of programmable interconnected 3D microfluidic networks. *Journal of Micromechanics and Microengineering* **2015,** *25* (2), 025018.

6. Dolega, M. E.; Wagh, J.; Gerbaud, S.; Kermarrec, F.; Alcaraz, J.-P.; Martin, D. K.; Gidrol, X.; Picollet-D'hahan, N., Facile bench-top fabrication of enclosed circular microchannels provides 3D confined structure for growth of prostate epithelial cells. *PloS one* **2014,** *9* (6), e99416.

7. Song, S.-H.; Lee, C.-K.; Kim, T.-J.; Shin, I.-c.; Jun, S.-C.; Jung, H.-I., A rapid and simple fabrication method for 3-dimensional circular microfluidic channel using metal wire removal process. *Microfluidics and nanofluidics* **2010,** *9* (2-3), 533-540.

8. (a) Wu, W.; Hansen, C. J.; Aragón, A. M.; Geubelle, P. H.; White, S. R.; Lewis, J. A., Direct-write assembly of biomimetic microvascular networks for efficient fluid transport. *Soft Matter* **2010,** *6* (4), 739-742; (b) Wu, W.; DeConinck, A.; Lewis, J. A., Omnidirectional printing of 3D microvascular networks. *Advanced Materials* **2011,** *23* (24); (c) Bhattacharjee,

T.; Zehnder, S. M.; Rowe, K. G.; Jain, S.; Nixon, R. M.; Sawyer, W. G.; Angelini, T. E., Writing in the granular gel medium. *Science advances* **2015,** *1* (8), e1500655; (d) Hinton, T. J.; Jallerat, Q.; Palchesko, R. N.; Park, J. H.; Grodzicki, M. S.; Shue, H.-J.; Ramadan, M. H.; Hudson, A. R.; Feinberg, A. W., Three-dimensional printing of complex biological structures by freeform reversible embedding of suspended hydrogels. *Science advances* **2015,** *1* (9), e1500758.

9. Lebel, L. L.; Aissa, B.; Khakani, M. A. E.; Therriault, D., Ultraviolet-Assisted Direct-Write Fabrication of Carbon Nanotube/Polymer Nanocomposite Microcoils. *Advanced Materials* **2010,** *22* (5), 592-596.

10. Guo, S. Z.; Gosselin, F.; Guerin, N.; Lanouette, A. M.; Heuzey, M. C.; Therriault, D., 3D Printing: Solvent-Cast Three-Dimensional Printing of Multifunctional Microsystems (Small 24/2013). *Small* **2013,** *9* (24), 4090-4090.

11. Hack, N.; Lauer, W. V., Mesh-Mould: Robotically Fabricated Spatial Meshes as Reinforced Concrete Formwork. *Architectural Design* **2014,** *84* (3), 44-53.

12. (a) Lee, J.; Paek, J.; Kim, J., Sucrose-based fabrication of 3D-networked, cylindrical microfluidic channels for rapid prototyping of lab-on-a-chip and vaso-mimetic devices. *Lab on a Chip* **2012,** *12* (15), 2638-2642; (b) Miller, J. S.; Stevens, K. R.; Yang, M. T.; Baker, B. M.; Nguyen, D.-H. T.; Cohen, D. M.; Toro, E.; Chen, A. A.; Galie, P. A.; Yu, X., Rapid casting of patterned vascular networks for perfusable engineered three-dimensional tissues. *Nature materials* **2012,** *11* (9), 768-774; (c) He, Y.; Qiu, J.; Fu, J.; Zhang, J.; Ren, Y.; Liu, A., Printing 3D microfluidic chips with a 3D sugar printer. *Microfluidics and nanofluidics* **2015,** *19* (2), 447-456.

13. Gravesen, P.; Branebjerg, J.; Jensen, O. S., Microfluidics-a review. *Journal of Micromechanics and Microengineering* **1993,** *3* (4), 168.

14. Stroock, A. D.; Dertinger, S. K.; Ajdari, A.; Mezić, I.; Stone, H. A.; Whitesides, G. M., Chaotic mixer for microchannels. *Science* **2002,** *295* (5555), 647-651.

15. (a) Dean, W.; Hurst, J., Note on the motion of fluid in a curved pipe. *Mathematika* **1959,** *6* (1), 77-85; (b) Dean, W., LXXII. The stream-line motion of fluid in a curved pipe (Second paper). *The London, Edinburgh, and Dublin Philosophical Magazine and Journal of Science* **1928,** *5* (30), 673-695.

16. (a) Sudarsan, A. P.; Ugaz, V. M., Multivortex micromixing. *Proceedings of the National Academy of Sciences* **2006,** *103* (19), 7228-7233; (b) Howell Jr, P. B.; Mott, D. R.; Golden, J. P.; Ligler, F. S., Design and evaluation of a Dean vortex-based micromixer. *Lab on a Chip* **2004,** *4* (6), 663-669; (c) Vanka, S.; Luo, G.; Winkler, C., Numerical study of scalar mixing in curved channels at low Reynolds numbers. *AIChE journal* **2004,** *50* (10), 2359-2368; (d) Jiang, F.; Drese, K.; Hardt, S.; Küpper, M.; Schönfeld, F., Helical flows and chaotic mixing in curved micro channels. *AIChE journal* **2004,** *50* (9), 2297-2305; (e) Wu, C.-Y.; Tsai, R.-T., Fluid mixing via multidirectional vortices in converging–diverging meandering microchannels with semi-elliptical side walls. *Chemical engineering journal* **2013,** *217*, 320-328; (f) Chen, J. J.; Shie, Y. S., Interfacial configurations and mixing performances of fluids in staggered curved-channel micromixers. *Microsystem technologies* **2012,** *18* (11), 1823-1833; (g) Scherr, T.; Quitadamo, C.; Tesvich, P.; Park, D. S.-W.; Tiersch, T.; Hayes, D.; Choi, J.-W.; Nandakumar, K.; Monroe, W. T., A planar microfluidic mixer based on logarithmic spirals. *Journal of Micromechanics and Microengineering* **2012,** *22* (5), 055019.

17. Berger, S.; Talbot, L.; Yao, L., Flow in curved pipes. *Annual review of fluid mechanics* **1983,** *15* (1), 461-512.

18. Zabielski, L.; Mestel, A., Steady flow in a helically symmetric pipe. *Journal of Fluid Mechanics* **1998,** *370*, 297-320.

19. Sudarsan, A. P.; Ugaz, V. M., Fluid mixing in planar spiral microchannels. *Lab on a Chip* **2006,** *6* (1), 74-82.

20. (a) Liu, K.; Yang, Q.; He, S.; Chen, F.; Zhao, Y.; Fan, X.; Li, L.; Shan, C.; Bian, H., A

high-efficiency three-dimensional helical micromixer in fused silica. *Microsystem technologies* **2013,** *19* (7), 1033-1040; (b) Kumar, V.; Aggarwal, M.; Nigam, K., Mixing in curved tubes. *Chemical Engineering Science* **2006,** *61* (17), 5742-5753.

21. Gad-el-Hak, M., The fluid mechanics of microdevices-the Freeman scholar lecture. *Transactions-American Society of Mechanical Engineers Journal of FLUIDS Engineering* **1999,** *121*, 5-33.

22. (a) Comesaña, J. F.; Otero, J. J.; García, E.; Correa, A., Densities and viscosities of ternary systems of water+ glucose+ sodium chloride at several temperatures. *Journal of Chemical & Engineering Data* **2003,** *48* (2), 362-366; (b) Chang, Y.; Myerson, A., The diffusivity of potassium chloride and sodium chloride in concentrated, saturated, and supersaturated aqueous solutions. *AIChE journal* **1985,** *31* (6), 890-894; (c) Vitagliano, V.; Lyons, P. A., Diffusion coefficients for aqueous solutions of sodium chloride and barium chloride. *Journal of the American Chemical Society* **1956,** *78* (8), 1549-1552; (d) Gladden, J.; Dole, M., Diffusion in supersaturated solutions. II. Glucose solutions. *Journal of the American Chemical Society* **1953,** *75* (16), 3900-3904.

23. Zhu, L.; Tretheway, D.; Petzold, L.; Meinhart, C., Simulation of fluid slip at 3D hydrophobic microchannel walls by the lattice Boltzmann method. *Journal of Computational Physics* **2005,** *202* (1), 181-195.

24. Ansari, M. A.; Kim, K.-Y., Shape optimization of a micromixer with staggered herringbone groove. *Chemical Engineering Science* **2007,** *62* (23), 6687-6695.

25. Farahani, R. D.; Chizari, K.; Therriault, D., Three-dimensional printing of freeform helical microstructures: a review. *Nanoscale* **2014,** *6* (18), 10470-10485.

26. Gelber, M. K.; Kole, M. R.; Kim, N.; Aluru, N. R.; Bhargava, R., Quantitative Chemical Imaging of Nonplanar Microfluidics. *Analytical chemistry* **2017,** *89* (3), 1716-1723.

27. Inglis, D. W., A method for reducing pressure-induced deformation in silicone

microfluidics. *Biomicrofluidics* **2010,** *4* (2), 026504.

Chapter 4

Uncertainty quantification for 3D printing system

4.1 Introduction

Additive manufacturing (AM) or 3D printing refers to processes that can fabricate a three-dimensional (3D) physical object from a digital computer-aided design (CAD) model by directly joining materials in a layer-by-layer fashion. The traditional manufacturing processes, in contrast, are subtractive in that a part is produced mainly by removing materials, often increasing material waste, and therefore production cost. Also, the manufacturing time of a subtractive process depends highly on the geometrical complexity of products. However, since additive manufacturing renders the product in a layer by layer fashion, complex geometrical products can be built without increasing the manufacturing time and/or costs. Due to these advantages, AM has been increasingly used to produce a wide range of parts and products, replacing traditional manufacturing processes.[1] Furthermore, AM even allows for creation of sophisticated geometries which would not be possible otherwise. For example, AM can be used to fabricate lightweight cellular structures to sustain large external loads. Highly ordered cellular structures result in high stiffness and toughness per unit weight and large surface to volume ratio. Many applications of cellular structures have been suggested including energy absorbing systems,[2] thermal applications,[3] and biomimetic materials.[4]

Despite significant advances in AM techniques, distinctive deviations still exist between the CAD model and the final printed product, resulting from various sources, such as digitization of 3D models, non-uniform material forming, and defects from the printing processes.[5] The staircase sidewall profile is one of the most prominent problems found in most

3D printed parts. As the use of AM gradually changes from prototyping to functional part production, accurate prediction of mechanical properties of 3D printed parts has become increasingly important. Recent research shows that dimensional accuracy, geometrical alignment, and surface roughness of micro- and nano-structures fabricated by AM techniques can result in large deviations of mechanical properties.[6] The impact of geometrical uncertainties on mechanical performance becomes more pronounced for micro-structures as the length scale of the 3D printed parts approaches the spatial deviations from manufacturing process. Previous research quantified the stiffness variations of 3D printed micro-lattice structures resulting from geometrical uncertainties.[6a] However, the geometrical differences are limited to the radial deviations, so the effects from the staircase sidewall profile and roughness have not been considered. To our knowledge, there is no previously reported work that took into account the actual deviation between planned and printed geometries to investigate the effect of topological uncertainties on the mechanical performance of 3D printed parts.

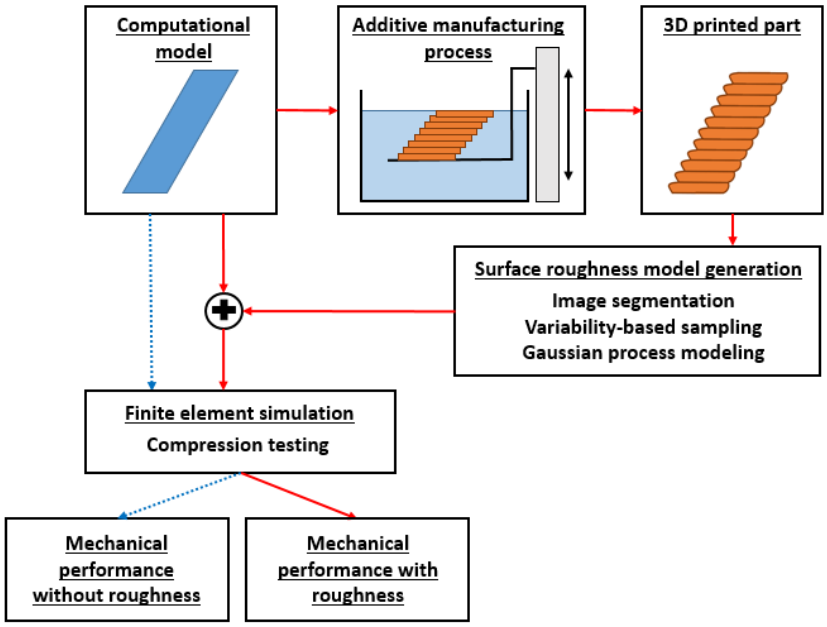

Figure 4.1 A probabilistic modeling framework for surface roughness estimation and mechanical behavior of a 3D printed geometry.

In this chapter, we present a probabilistic modeling framework that can predict the spatial variations of printed geometry using images of 3D-printed structures. The details of this framework are shown in Figure 4.1. We limit our interest to the spatial variations of a single strut as it is a building block of various types of 3D micro-lattices and the load bearing characteristics of a single strut can determine the mechanical behavior of the overall lattice structure. From the CAD model, the 3D printed part is manufactured through the additive manufacturing process. We extract the surface roughness information in the sidewall profile of the 3D printed part resulting from the layer-by-layer manufacturing process, and generate a probabilistic surface roughness model. To generate the probabilistic model, we perform three steps: 1) image segmentation using the level set method to extract the sidewall profiles of the printed geometry, 2) variability-based sampling to reduce the size of the data set from 1), and 3) Gaussian process model for spatial uncertainty. The surface roughness model is incorporated with the CAD geometry, so that we can simulate the compression testing with/without surface roughness of the struts. The red arrows in Figure 4.1 indicate the information flow to calculate the mechanical performance of a single strut with surface roughness, and the blue arrows display the information flow without accounting for the roughness of the strut.

We demonstrate our methodology for variability-based sampling and Gaussian process modeling with a controlled test problem. The test problem is carefully selected to represent the spatially varying profiles. After the verification process, we apply it to 3D printed struts to generate a spatial variation model of an actual 3D printed geometry. In order to visualize the effect of spatial deviations on the mechanical behavior of 3D printed products, the struts' stiffness and maximum von Mises stress under compression are compared with those of the struts without spatial deviations. In addition, the effective elastic modulus of the unit cell structure with and without spatial deviations is also studied.

4.2 Materials and methods

4.2.1 Image segmentation with level sets

The accuracy of data-driven stochastic model for spatial uncertainties depends on the experimental characterization data. Although, profilometry is a fast and simple method to measure the spatial profiles, the usage of profilometry is limited by its dimensional accessibility.[7] Therefore, we employ an image-based technique to extract the spatial variation of 3D printed products. The basic idea is collecting sidewall profile data of 3D printed struts from multiple sample images, and extracting the data set that can be used to quantify the spatial variations using image segmentation. This image-based technique can be applied to any spatially varying field obtained from any imaging technique.

Image segmentation is a partitioning process that groups clusters of pixels of a digital image based on their colors, intensities, textures, etc. in order to extract useful information from the image.[8] Various techniques have been proposed for segmenting given images.[8-9] Among these, one of the simplest and mostly widely used technique for image segmentation is thresholding. Thresholding separates pixels whose gray scale level is higher than a critical value from the background: the critical value for the thresholding is defined by the image's gray-level histogram.[8] However, some disadvantages of thresholding have been also reported such as susceptibility to pixel noise and the extract profile possibly not being a closed contour due to lack of consideration of spatial characteristics.[10] To mitigate this, we use the level set method in order to extract the profiles of objects in the image.[11] In the level set method, a higher dimensional function called the level set function (ϕ) is defined to describe the contour. This contour evolves towards the objects' boundaries in the image based on the predefined constraints, such as differences or gradients of pixel intensities. From the evolving level set function, the contours are given by the zero level set, $C = \{(x, y) | \, \phi(x, y) = 0\}$, which evolves towards the objects' boundaries.

Let $\Omega \subset R^2$ be the domain inside an image, and $I(\mathrm{x},\mathrm{y})$ represent the intensity of pixel at the pixel location (x, y). The general form of the energy function E in the level set method is shown below:[12]

$$E = \lambda_o \int_{\Omega} |\, I(x,y) - u_o \,|^2 \, H(\phi(x,y))dxdy + \lambda_b \int_{\Omega} |\, I(x,y) - u_b \,|^2 \, (1 - H(\phi(x,y)))dxdy + \gamma \int_{\Omega} \mathrm{g}(\phi(x,y)) \,|\, \nabla \phi(x,y) \,|\, dxdy \tag{4.1}$$

where u_o and u_b are the pixel intensity averages inside the contour and in the background region, respectively. λ_o, λ_b, and γ are non-negative weighting factors. A smoothing function $\mathrm{g(x)} = (1 + \exp((\mathrm{x} - \xi)/L))^{-1}$ is chosen for robustness of the algorithm. L defines the smoothing length and ξ locates the center of the smoothing function. The Heaviside function (H) is used to differentiate the object Ω_o and the background Ω_b. With the fixed level set function, u_o and u_b can be obtained by:

$$u_o = \frac{\int_{\Omega} I(x,y) H(\phi(x,y))dxdy}{\int_{\Omega} H(\phi(x,y))dxdy}$$
$$u_b = \frac{\int_{\Omega} I(x,y)(1 - H(\phi(x,y)))dxdy}{\int_{\Omega} (1 - H(\phi(x,y)))dxdy} \tag{4.2}$$

Given u_o and u_b, the energy function E can be minimized by a standard gradient descent algorithm.[12] The physical meaning of each term in Equation (4.1) is as follows: The first term matches the average pixel intensity inside of the contour with the pixel intensity of

objects by minimizing its mean-squared error. Similarly, the second term matches the pixel intensity of background in the image. The third term regulates the smoothness of the contour, so a higher weight of this term would mean smoothing the contour. The initial condition of the level set function is given by the threshold pixel intensities.

4.2.2 Variability-based sampling and bisection method

The extracted boundaries from image segmentation are a uniformly distributed data set, showing the edge profile. This data can be used for the Gaussian process model, but since the number of data points in the set is proportional to the number of hyperparameters to be fitted, an efficient sampling of the data set is required to reduce the computational cost and improve the convergence rate. To determine the sampling locations along the profile $y(x)$, the local variability, σ_y^2, is defined to calculate the probability of sampling at each location, $\Pr(x)$:[13]

$$\Pr(x) \propto \sigma_y^2(x) = \frac{1}{n_x - 1} \sum_{x' \in R(x)} \left(\frac{y(x') - \overline{y}(x)}{x' - x} \right)^2 \tag{4.3}$$

where x' is a location within the region around x, $\overline{y}$ is the local mean of the profile values in the region $R(x)$, and n_x is the number of measurement locations in the region. The intent behind the variability-based sampling is that the regions where the profile varies more frequently need to have more sampling locations, so that the details within this region can be captured properly. Using the probability distribution for sampling defined in Equation (4.3), the sampling locations with higher local variability will have a higher possibility to be selected as the initial measurements.

In addition to the variability-based sampling, we also employ an iterative bisection algorithm: if a certain region between two selected measurement locations has a large deviation between the estimated mean and the mean from realizations, we add an additional measurement point in the middle of the region to improve the match. This process is repeated until the deviations in the entire region are lower than the threshold value.

4.2.3 Gaussian process modeling

In this study, we employ projection micro-stereolithography (PμSL) as a model AM process.[14] The layer-by-layer nature of the process inevitably gives rise to a staircase-like sidewall profile of the part, which results in a geometric difference between the 3D printed part and the planned geometry (or the 3D computer model). Furthermore, the angle between the substrate and the printed strut can affect this geometric difference. This problem is universal and found in most AM processes. In order to quantify the deviation, we take the sidewall profiles of the 3D printed object using a digital camera attached to a microscope. We assume that the extracted edge profiles of 3-D printed objects result from two parts: 1) consistent curing behavior from the printing apparatus (consistent deviation between the planned geometry and the actual printed geometry), 2) stochastic roughness from 3D printing process caused by inherent uncertainties, such as light scattering, projection not perfectly focused on the curing plane, uncontrolled external environmental factors, etc. After separating the effects from the two factors mentioned above, we focus on the second part, the spatially-varying stochastic roughness, which is not a function of the printed angle.

Stochastic roughness is often represented by a random process, defined as a collection of random variables in space or time. In this work, we assume that the random process behind spatial roughness is represented by a Gaussian process.[15] The advantage of using a Gaussian process is that the random process is fully described by the mean and covariance functions so

that the full probabilistic prediction as well as the estimation of uncertainty in the prediction can be obtained.

Thus, we define the uncertainty in the sidewall profile as the roughness (*d*) and assume that this roughness is the realization of a Gaussian process (*f*). Gaussian process is a statistical model that produces a set of random variables; the finite selection of the random values within the set follows a multivariate Gaussian distribution.[15] The Gaussian process is fully described in terms of its mean M and covariance C and its realization is also fully specified by $M(X)$ and $C(X,X)$, where X is the domain of the realization.[16] The stationary Gaussian process model for roughness is defined as:

$$\begin{aligned} &f \mid M, C \sim GP(M, C) \\ &d \mid M, C \sim N(M(X), C(X, X)) \\ &M : X, \alpha, t_M \rightarrow \sum_i \alpha_i B_{i,k}(X; t_M) \\ &C : x, x', \nu, \phi, \theta \rightarrow Matern(x, x', \nu, \phi, \theta) \end{aligned} \tag{4.4}$$

where $B_{i,k}$ is the B-spline basis function of order k and α_i is the corresponding weight factor. t_M is the knot vector for the mean function.[17] The B-spline representation is used as the mean function to model the local variability of roughness. This is particularly useful when the shape of mean function is not known *a priori*. The Matérn covariance is used because it represents a diverse class of covariance functions that belong to the exponential family, which is commonly used to model physical stochastic process.[15] The Matérn covariance has three hyperparameters, ν, ϕ, θ, that control its differentiability, correlation length, and amplitude, respectively.

Using the sampled data from the variability-based sampling and bisection algorithm, we perform Bayesian estimation to obtain the estimates for the unknown parameters in Equation (4.4). If prior information about the distribution of the unknown parameters exists,

it can be incorporated into the prior probability density functions (PDFs) of the corresponding unknown parameters. On the other hand, the non-zero values for parameters in the Matérn covariance function can be included if there is no prior information about the parameters in the mean and covariance functions.[18]

4.3 Results and discussions

4.3.1 Verification for GP modeling and sampling algorithm

We present a test problem to illustrate and verify our Gaussian process modeling with the variability-based sampling and bisection algorithm. Equation (4.5) is the mathematical form of the given mean function q:

$$q(x) = \sin(2(x-0.9)^4)\cos(x-0.2) + \frac{1}{2}(x-0.5)^3 \tag{4.5}$$

The linear slope between the starting and ending points of the function is removed since roughness is the main focus. We use the function in Equation (4.5) with a larger roughness frequency in the region $x \in [-1,0]$ than in the region $[0,1]$ to test whether our algorithm can capture the correct behavior of spatial roughness when its characteristics are not uniform over the entire domain. A Matérn covariance function with the parameters: ν=2, ϕ=2, , θ=0.4 is used to generate the spatial roughness. We generate realizations of this random process and sample these realizations at uniform or non-uniform locations for a total of 61 measurement locations. The sampled data is used as the input for estimation, where we try to reconstruct the parameters of the actual stochastic process from which the data originated. We assign the following prior PDFs for the unknown parameters:

$$\begin{aligned} &\alpha_i \sim Uniform[-10,10] \\ &\nu \sim Uniform(1) \\ &\phi \sim Exponential(1) \\ &\theta \sim Exponential(1) \end{aligned} \tag{4.6}$$

The prior PDFs can be specifically chosen to incorporate any knowledge we may have on the values of the unknown parameters or can be left sufficiently vague in the absence of such information. Using 500 realizations of the given random process that are sampled at the

given locations, we generate the joint posterior distribution of the parameters and pick 1000 samples from it by using the Markov Chain Monte Carlo (MCMC) method with a burn-in of 30,000 and a thinning factor of 10.[7] The open-source Bayesian analysis package PyMC[19] is used to perform Monte Carlo sampling in order to estimate their posterior PDFs.

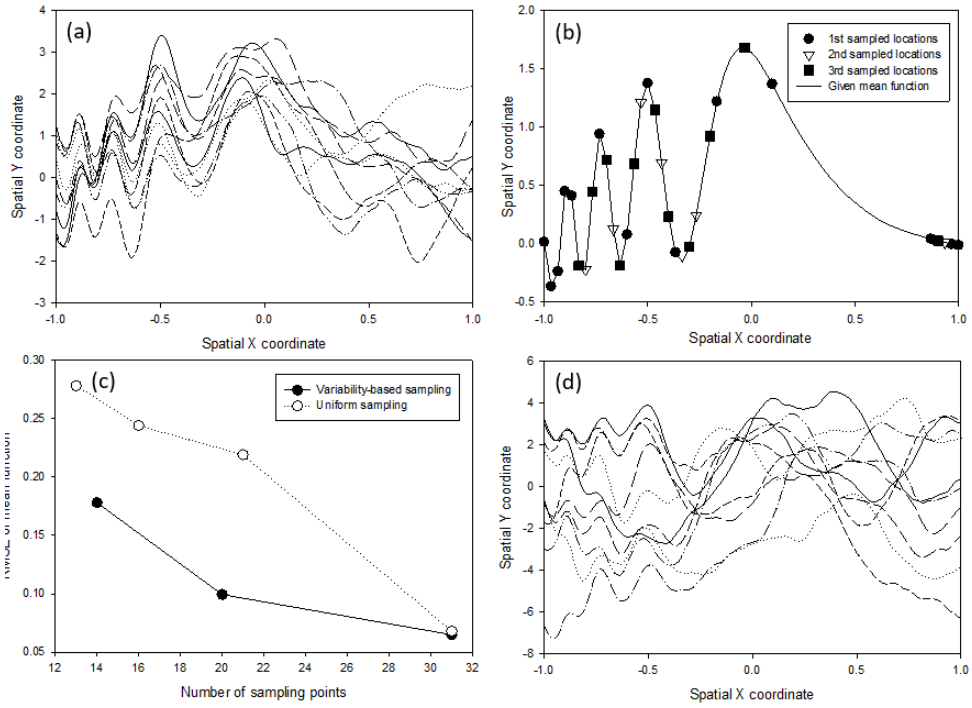

Figure 4.2 Given and estimated stochastic processes. (a) 10 realizations from the given model. (b) Given mean function (solid line) and sampled points in 1st (circle), 2nd (triangle), and 3rd (rectangle) runs after variability-based sampling algorithm. (c) RMSE of the mean function from uniform and variability-based sampling algorithm. (d) 10 sampled realizations from the estimated Gaussian process model.

Figure 4.2 (a) shows 10 realizations from the given stochastic process. The sampled points in 1st (circles), 2nd (triangles), and 3rd (rectangles) time runs of non-uniform sampling are also shown in Figure 4.2 (b). The 1st sample points based on the local variability capture

the high frequency roughness in the left sidewall effectively. However, it misses some details on the left sidewall as well as on the right sidewall. The lack of sampling points is compensated in 2nd and 3rd bisection steps by placing additional sampling points, reducing the deviation between the mean function calculated from all realizations and the estimated mean function. To visualize the effectiveness of variability-based sampling and the bisection algorithm, the root mean square error (RMSE) between the estimated mean and the mean from realizations is calculated and compared in two different sampling cases: 1) proposed variability-based sampling, 2) uniform sampling. The result is shown in Figure 4.2 (c). The x-axis is the number of sampling points, and the y-axis is the RMSE value. Because of the efficient placement of measurement locations, the RMSE in non-uniform sampling is much smaller than the uniform sampling result with equal number of sampling points. In addition, as the sampling locations are increased the RMSE is reduced, but the RMSE reduces much faster in the variability-based method. When the sampling locations is almost half of the total measurement locations, the RMSEs in both methods are the same. Therefore, we can conclude that the variability-based sampling and the bisection algorithm is a more attractive option for effective allocation of computing power and resources. Figure 4.2 (d) shows 10 sampled realizations from the estimated Gaussian process model.

In addition to the comparison of the mean function, the estimated parameters with respect to the number of sampling points are shown in Table 4.1. There are three parameters in the Matérn covariance function, and the given values are denoted in the parentheses. Unlike the deviations in the mean function, the estimated parameters do not depend strongly (within a 5% error) on the number of sampling points.

Table 4.1 Estimated hyperparameters for test problem. The given values are denoted in the parentheses.

	ν (2)	**ϕ (2)**	**θ (0.4)**
1st sampled locations (14 points)	2.011±0.027	2.052±0.028	0.416±0.012
2nd sampled locations (20 points)	1.978±0.025	2.063±0.030	0.418±0.009
3rd sampled locations (31 points)	1.971±0.016	2.055±0.029	0.415±0.007

4.3.2 Extracting profiles from 3D printed strut images

Gaussian process modeling with non-uniform sampling algorithm is applied to the sidewall profiles of 3D printed struts. Figure 4.3 (a-c) show the CAD geometries of struts in 3 different printing angles (90°, 75°, and 60°) and printing directions. The layer thickness is 80 in the pixel units. The sidewall profiles of multiple 3D-printed struts with different angles (90°, 75°, and 60°) are shown in Figure 4.3 (d-f). The sidewall profile consists of multiple layers printed repeatedly layer by layer, and we assume that each printed layer is generated from an independent event and not related to the neighboring layers. There are three parameters in Eq. (1) that can be reduced by considering the two ratios, λ_b/λ_o and γ/λ_o. We manually segmented one printed layer in the image and varied the two ratios to find the optimized parameter values, giving the best match with the manually segmented edge. Figure 4.3 (g-i) show the binary masks of the images after segmentation, where the white pixels represent the segmented region of the strut and the black pixels are the background region. Due to the smooth intensity gradient from the center to the edge of the image, the segmentation at the edges of the images are inaccurate for 75° and 60° cases. This artifact from the background inhomogeneity can be easily removed by measuring and compensating the intensity gradient in the background. In order to minimize the manual intervention, the compensation is not applied in this study. A more systematical approach for reducing the effect from the local inhomogeneity can be found in.[20]

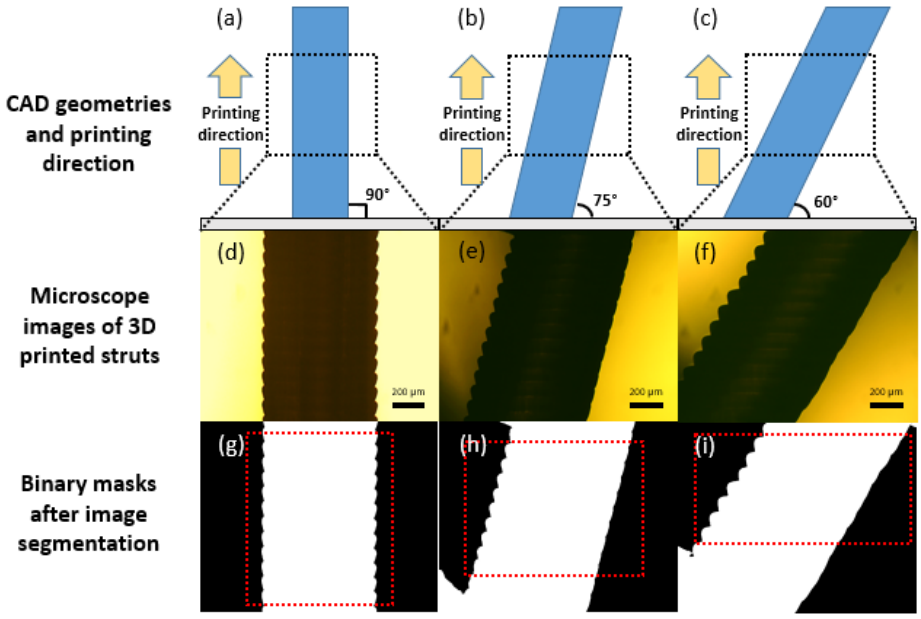

Figure 4.3 Microscope images and corresponding binary images of 3D printed struts. (a-c) CAD geometries of struts in different printing angles (90°, 75°, and 60°). (d-f) Microscope images of 3D printed struts (90°, 75°, and 60°). (g-i) Binary masks after image segmentation (90°, 75°, and 60°). The sidewall profiles in the red box (dotted line) are used for characterizing the spatial uncertainty.

The edge profile can be extracted by collecting the outer most pixels in the left and right sidewalls of binary masks. Figure 4.4 (a-b) shows the extracted edge profiles in the left and right sidewalls of each printed layer, respectively. Like the test case, the mean of all observations is separated from the roughness, so that the roughness is independent of the printed angle. The mean trends extracted from all the observations and the roughness are shown in Figure 4.4 (c-f).

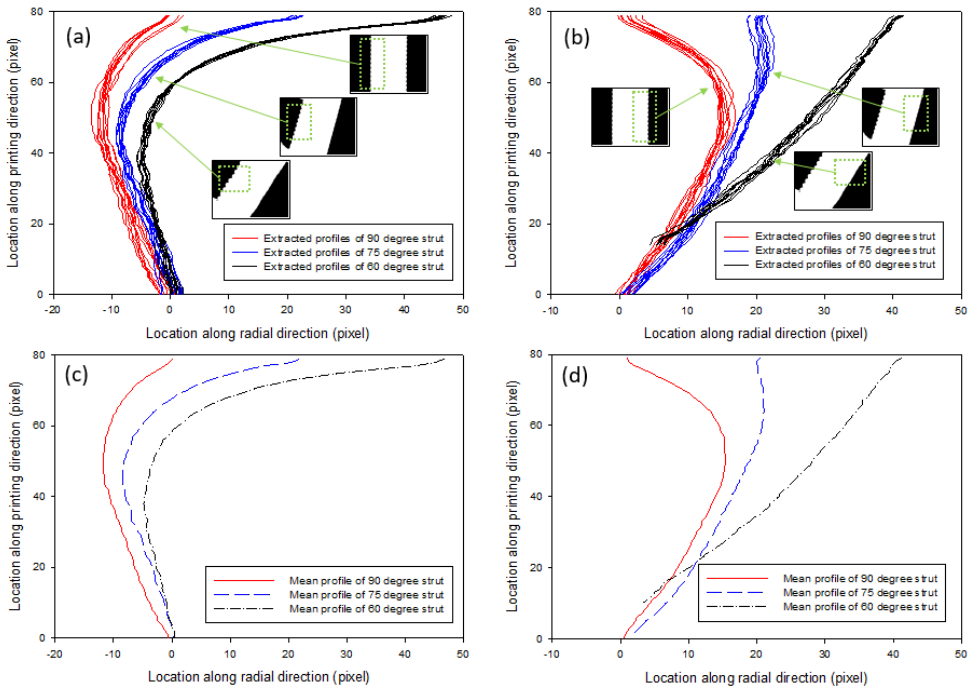

Figure 4.4 Extracted sidewall profiles of 3D printed struts. (a) The extracted left-sidewall profiles in different angles (90°, 75°, and 60°). (b) The extracted right-sidewall profiles in different angles (90°, 75°, and 60°). (c) Extracted left-sidewall mean profiles in different angles (90°, 75°, and 60°). (d) Extracted right-sidewall mean profiles in different angles (90°, 75°, and 60°). (e) Extracted left-sidewall roughness profiles after clean-up. (f) Extracted right-sidewall roughness profiles after clean-up.

Unlike the test case, we do have the prior information on the distribution of some of the hyperparameters, i.e., the amplitude and scaling parameters of covariance function, as given in Equation (4.7). Based on the roughness amplitude from observations, the upper limit on the prior distribution of the amplitude parameter in the covariance function is 5. In addition, the maximum correlation length is limited up to the height of one printed layer.

$$\begin{aligned} &\alpha_i \sim Uniform[-10,10] \\ &\nu \sim Uniform[1,3] \\ &\phi \sim Uniform[0,5] \\ &\theta \sim Uniform[0,80] \end{aligned} \tag{4.7}$$

10 realizations from the estimated stochastic model are shown in Figure 4.5. Like the observations from the extracted profiles of actual struts, the fluctuations are distributed uniformly over the domain, which shows the characteristics of the stationary Gaussian process.

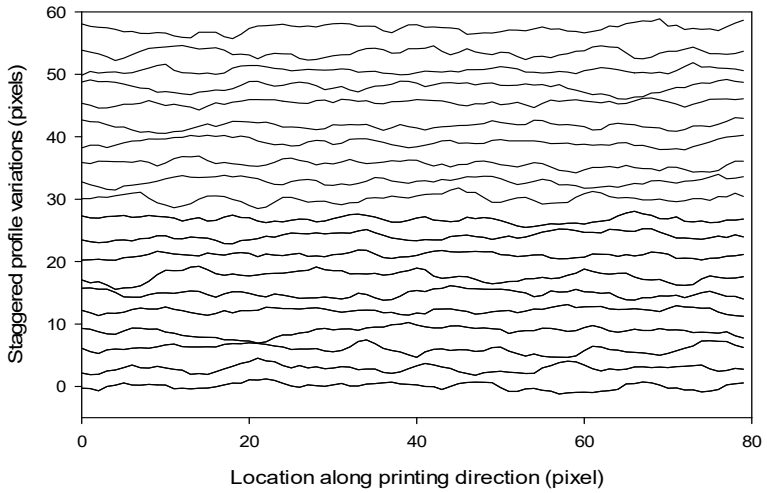

Figure 4.5 10 sampled realizations from the estimated Gaussian process model.

4.3.3 Effect of spatial uncertainty on the mechanical behavior of 3-D printed struts

To see the effect of spatial uncertainty on the mechanical properties of 3D printed struts, a compression test is performed with three different geometries of struts: 1) planned geometry from CAD file, 2) printed geometry including mean deviation and roughness from Gaussian process modeling, and 3) mean-matched smooth geometry with 2). The material stress-strain relation is required to perform the compression test. Figure 4.6 (a) shows the stress-strain curve obtained from a uniaxial compression test for the test specimen. The material used for the compression test is poly(ethylene glycol) diacrylate (PEGDA) (molecular weight=250). Based

on the experimental result, the neo-Hookean model for the hyperelastic material (Equation (3.9)) is fitted to extract the scaling factor between stress and strain.

$$\sigma = \mu\left(\lambda - \frac{1}{\lambda^2}\right) \tag{4.8}$$

σ is the stress, λ is the stretch ratio, and μ is the shear modulus of material. The fitted value of μ is ~36.1 MPa for the PEGDA, and the fitted line is displayed as dotted line in Figure 4.6 (a).

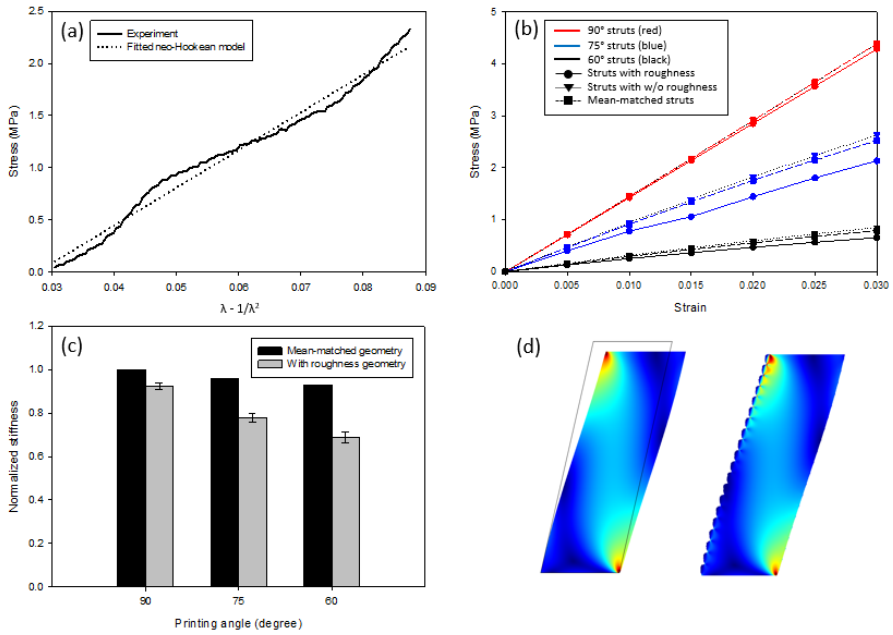

Figure 4.6 Compression test results of 3D printed struts. (a) Stress-strain curve for PEGDA sample from experiment (solid line) and fitted neo-Hookean model (dotted line). (b) Stress-strain curve for 3D printed struts of different printing angles (90°, 75°, and 60°) with roughness, without roughness, and mean-matched cases. (c) Normalized effective stiffness of mean-matched geometry and with-roughness cases in different printing angles (90°, 75°, and 60°). (d) Von Mises stress distributions with-roughness and CAD geometries

Figure 4.6 (b) shows the stress-strain curves of 9 different cases: 3 different printing angles (90°, 75°, and 60°), and in each printing angle, there exist 3 different cases (strut with roughness, strut without roughness, and mean-matched strut). The thickness of the strut in the CAD file is 800 μm, and the thicknesses of struts in the mean-matched geometries are ~754 μm, ~754 μm, and 760 μm for 90°, 75°, and 60°, respectively. The height of struts is 2000 μm for all cases. The slope of the stress-strain curve is the strut's stiffness. The slope of all stress-strain curves are grouped in 3 depending on its printing angle, and there exist a slope deviation because of the existence of spatial deviation. The decrease of slope can be noticed in the strut with roughness and mean-matched strut, qualitatively.

To understand the effect of spatial deviation on the struts' stiffness quantitatively, the stiffness of mean-matched and with-roughness struts are normalized with the stiffness of strut without roughness as shown in Figure 4.6 (c). The change in the effective stiffness of mean-matched geometry is not significant (less than 7% of the stiffness of the CAD geometry) when the printing angle changes from 90° to 60°. However, when the geometry has roughness, the stiffness reduces to 70% of the CAD case when the printing angle is 60°. The reduction in stiffness is expected since the roughness decreases the cross-sectional area of each strut, resulting in the reduction of stiffness of the strut. However, we can see that the roughness effect is more pronounced than reducing the cross-sectional area when we compare the results with the mean-matched cases.

In addition, we compare the maximum value of von Mises stress in the three cases. Table 4.2 shows that the maximum von Mises stresses of mean-matched geometry strut and strut with roughness divided by the maximum von Mises stress of the CAD geometry. As shown in Figure. 4.6 (d), local stress concentrations are observed near the rough profiles due to spatial uncertainty. However, this local concentration of stress is not observed in the mean-matched case or the CAD geometry case, where the sidewall profiles are smooth. The amount

of stress concentration is three times higher than the smooth cases. Therefore, it is essential to consider spatial uncertainties in the geometry to accurately predict the mechanical behavior of struts.

Table 4.2 The normalized maximum von Mises stress of mean-matched strut and with roughness strut with respect to CAD geometry in different printed angles.

	90°	**75°**	**60°**
Mean-matched geometry	0.975	0.955	0.947
With-roughness geometry	3.410	3.752	3.273

4.3.4 Effect of spatial uncertainty on the mechanical behavior of unit cell structure

As a basic building block of the microlattice structure, several different unit cell structures have been proposed and their mechanical properties have been tested.[21] The spatial variations discussed in the previous sections are applied to the square unit cell structure to understand the effect of spatial variation on the mechanical behavior.[22] This square unit cell structure consists of horizontal, 45°, 90° printed struts as shown in the inset of Figure 4.7.

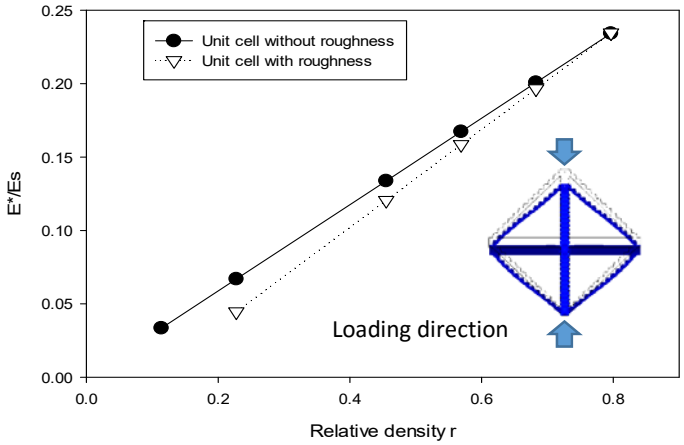

Figure 4.7 Compression test results of 3D printed unit cell structures: normalized effective stiffness of unit cells with and without spatial roughness.

The effective elastic modulus of square unit cell with roughness is calculated and compared with the solid structure. Here, the solid structure regards to the unit cell structure without any voids. Figure 4.7 shows the normalized stiffness values as a function of relative density of unit cells. The relative density in the X-axis is density ratio between the printed lattice structure over the solid structure. For the planar unit cell, this is the same as the area ratio between the printed lattice structure and the solid structure. The Y-axis is the ratio of the effective elastic modulus between the solid and the lattice structure. The solid line in the figure is the analytical result taken from the reference paper,[22] and the dotted line shows the square unit cell structure with spatial roughness. When the relative density is around 80% of the solid case, the effective elastic modulus of the unit cell with roughness is almost the same as (95%) that of the solid structure. However, as the relative density decreases, the deviation due to the spatial roughness becomes significant because the magnitude of spatial roughness become comparable to the thickness of struts. Based on the fact that most of lattice structure has the relative density of around 0.3 or less, the spatial roughness reduces the effective elastic modulus more than 30% in this relative density range. Therefore, when the magnitude of spatial roughness is comparable with the thickness of struts of unit cell structure, the spatial roughness should be taken into consideration.

4.4 Conclusion

This chapter presents a general method to model spatial variations of 3D printed products from their sidewall profile images. Specifically, this can be achieved using 3 approaches: 1) Gaussian process modeling using Bayesian network and MCMC sampling, 2) level set method for image segmentation, and 3) variability-based sampling algorithm. This method is verified with the test problem and applied to the real 3D printed products. The results show that the spatial roughness needs to be considered when the spatial roughness is comparable with the dimension of 3D printed structures. The proposed method is not limited to the 3D printed products, and it can be applied to other problems where spatial variations are important.

4.5 References

1. (a) Melchels, F. P.; Feijen, J.; Grijpma, D. W., A review on stereolithography and its applications in biomedical engineering. *Biomaterials* **2010,** *31* (24), 6121-6130; (b) Alapan, Y.; Hasan, M. N.; Shen, R.; Gurkan, U. A., Three-dimensional printing based hybrid manufacturing of microfluidic devices. *Journal of Nanotechnology in Engineering and Medicine* **2015,** *6* (2), 021007.

2. (a) Schaedler, T. A.; Ro, C. J.; Sorensen, A. E.; Eckel, Z.; Yang, S. S.; Carter, W. B.; Jacobsen, A. J., Designing metallic microlattices for energy absorber applications. *Advanced Engineering Materials* **2014,** *16* (3), 276-283; (b) Frenzel, T.; Findeisen, C.; Kadic, M.; Gumbsch, P.; Wegener, M., Tailored Buckling Microlattices as Reusable Light-Weight Shock Absorbers. *Advanced Materials* **2016**; (c) Tancogne-Dejean, T.; Spierings, A. B.; Mohr, D., Additively-manufactured metallic micro-lattice materials for high specific energy absorption under static and dynamic loading. *Acta Materialia* **2016,** *116*, 14-28.

3. (a) Roper, C. S.; Fink, K. D.; Lee, S. T.; Kolodziejska, J. A.; Jacobsen, A. J., Anisotropic convective heat transfer in microlattice materials. *AIChE journal* **2013,** *59* (2), 622-629; (b) Maloney, K. J.; Fink, K. D.; Schaedler, T. A.; Kolodziejska, J. A.; Jacobsen, A. J.; Roper, C. S., Multifunctional heat exchangers derived from three-dimensional micro-lattice structures. *International Journal of Heat and Mass Transfer* **2012,** *55* (9), 2486-2493.

4. Warnke, P. H.; Douglas, T.; Wollny, P.; Sherry, E.; Steiner, M.; Galonska, S.; Becker, S. T.; Springer, I. N.; Wiltfang, J.; Sivananthan, S., Rapid prototyping: porous titanium alloy scaffolds produced by selective laser melting for bone tissue engineering. *Tissue engineering part c: Methods* **2008,** *15* (2), 115-124.

5. (a) Ahn, D.; Kim, H.; Lee, S., Surface roughness prediction using measured data and interpolation in layered manufacturing. *Journal of materials processing technology* **2009,** *209* (2), 664-671; (b) ANCĂU, M.; CAIZAR, C., The Optimization of Surface Quality in Rapid

Prototyping.

6. (a) Hasan, R. Progressive collapse of titanium alloy micro-lattice structures manufactured using selective laser melting. University of Liverpool, 2013; (b) Meza, L. R.; Greer, J. R., Mechanical characterization of hollow ceramic nanolattices. *Journal of Materials Science* **2014,** *49* (6), 2496-2508.

7. Alwan, A.; Aluru, N., Data-driven stochastic models for spatial uncertainties in micromechanical systems. *Journal of Micromechanics and Microengineering* **2015,** *25* (11), 115009.

8. Pal, N. R.; Pal, S. K., A review on image segmentation techniques. *Pattern recognition* **1993,** *26* (9), 1277-1294.

9. (a) Shapiro, L.; Stockman, G. C., Computer vision. 2001. *ed: Prentice Hall* **2001**; (b) Cremers, D.; Rousson, M.; Deriche, R., A review of statistical approaches to level set segmentation: integrating color, texture, motion and shape. *International journal of computer vision* **2007,** *72* (2), 195-215.

10. Sahoo, P. K.; Soltani, S.; Wong, A. K., A survey of thresholding techniques. *Computer vision, graphics, and image processing* **1988,** *41* (2), 233-260.

11. Osher, S.; Sethian, J. A., Fronts propagating with curvature-dependent speed: algorithms based on Hamilton-Jacobi formulations. *Journal of computational physics* **1988,** *79* (1), 12-49.

12. Chan, T. F.; Vese, L. A., Active contours without edges. *Image processing, IEEE transactions on* **2001,** *10* (2), 266-277.

13. (a) Anderson, A.; Wang, G.; Gertner, G., Local variability based sampling for mapping a soil erosion cover factor by co-simulation with Landsat TM images. *International Journal of Remote Sensing* **2006,** *27* (12), 2423-2447; (b) Jin, R.; Chang, C.-J.; Shi, J., Sequential measurement strategy for wafer geometric profile estimation. *IIE Transactions* **2012,** *44* (1),

1-12.

14. (a) Sun, C.; Fang, N.; Wu, D.; Zhang, X., Projection micro-stereolithography using digital micro-mirror dynamic mask. *Sensors and Actuators A: Physical* **2005,** *121* (1), 113-120; (b) Zheng, X.; Deotte, J.; Alonso, M. P.; Farquar, G. R.; Weisgraber, T. H.; Gemberling, S.; Lee, H.; Fang, N.; Spadaccini, C. M., Design and optimization of a light-emitting diode projection micro-stereolithography three-dimensional manufacturing system. *Review of Scientific Instruments* **2012,** *83* (12), 125001.

15. Rasmussen, C. E., Gaussian processes for machine learning. **2006**.

16. Cressie, N., Statistics for spatial data: Wiley series in probability and statistics. *Wiley-Interscience New York* **1993,** *15*, 16.

17. De Boor, C., *A practical guide to splines*. Springer-Verlag New York: 1978; Vol. 27.

18. Alwan, A.; Aluru, N. R., A nonstationary covariance function model for spatial uncertainties in electrostatically actuated microsystems. *International Journal for Uncertainty Quantification* **2015,** *5* (2).

19. Patil, A.; Huard, D.; Fonnesbeck, C. J., PyMC: Bayesian stochastic modelling in Python. *Journal of statistical software* **2010,** *35* (4), 1.

20. Wang, X.-F.; Huang, D.-S.; Xu, H., An efficient local Chan–Vese model for image segmentation. *Pattern Recognition* **2010,** *43* (3), 603-618.

21. Gibson, L. J.; Ashby, M. F., *Cellular solids: structure and properties*. Cambridge university press: 1999.

22. Zhang, Y.; Qiu, X.; Fang, D., Mechanical properties of two novel planar lattice structures. *International Journal of Solids and Structures* **2008,** *45* (13), 3751-3768.

Chapter 5

Uncertainty quantification for die casting process

5.1 Introduction

Die casting manufacturing process is a variation of metal casting where the molten metal is injected into a mold cavity that has the desired shape of the product. The main advantages of die casting are 1) excellent dimensional accuracy, 2) rapid production speed, and 3) a wide range of metals such as aluminum, copper, lead, magnesium, and zinc alloys as well as various composite materials can be used. Due to these advantages, die casting has been widely used to produce various kinds of products, and approximately 475 die casters exist in North America with sales of $ 8 billion.[1] Despite significant use of die casting process in the industry, the design and process control of die casting products still relies on a design-make-test approach. As the complexity of the product increases, the time and cost for optimizing design parameters by a trial-and-error approach can increase significantly. Also, there exists a significant lack of understanding of uncertainties that lead to high variability of product performance.

Computer simulation has played an important role in guiding physical experimentation to confirm and improve the performance of a product. Recent advances in computing power have paved way for computational prototyping, resulting in a reduction of the manufacturing cost and improvement of product quality, performance, and reliability. This led to the idea of "virtually-guided certification." Virtually-guided certification employs a computational framework, including quantification of uncertainties, that provides simulation results with high reliability so that it can be used in the design and optimization of manufacturing processes.

In the case of die casting process, this requires an understanding of the multiphysics and multiscale phenomena involved in the die casting processes as well as characterizing and quantifying various uncertainties in the die casting processes.

This framework requires development of a system of sub-modules that consist of integrating information from experiments, computational models, and extensive verification & validation framework. The verification framework is the systematic verification procedure that confirms the fact that the computational model produces the right results. This is done by using the published data or the simplified problem that has the analytical solution. The validation framework confirms the fact that our computational model yields the physically correct results. This can be done by comparing the simulation results with the experimental results. In addition to these framework, UQ framework can be incorporated for several reasons: 1) Identifying the key uncertainties in the process. 2) Developing stochastic models for identified uncertainties. 3) Establishing validation framework with uncertainties. The proposed modeling framework in this study is shown in Figure 5.1.

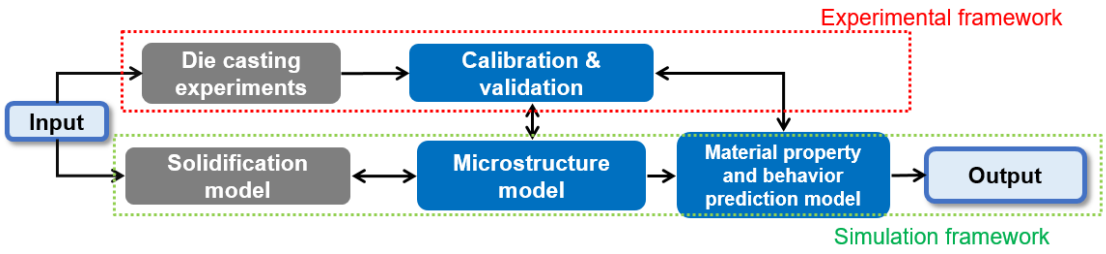

Figure 5.1 "Input parameters-manufacturing process-product property" framework. The experimental part and the simulation part are displayed in the red and green boxes, respectively. Details of each step are described in the context. The steps in this study are colored in blue.

The input node stands for the input parameters in the experiments, such as the die temperature, liquid metal temperature, shot rate, pressure, components of liquid metal, and so on. The upper part of the framework is the experimental framework, which is related to the actual die casting process in the industry. Die casting experiment is performed in the collaborating die casting company and the specimens produced in the company are used for the calibration and validation framework. From the specimens, the microstructure information and the mechanical property data are obtained for calibration and validation of the predictive models proposed in this study. The lower part of the framework is the simulation framework. The solidification model is the computational model that predicts the solidification process of liquid metal inside the die. The microstructure model is the predictive model that estimates the microstructure information, such as phase volume fraction, orientation, sizes, distribution, primary dendrite arm spacing (PDAS), secondary dendrite arm spacing (SDAS), depending on the solidification conditions. The empirical model that predicts PDAS/SDAS based on the solidification parameters such as temperature and temperature gradients. The material property and behavior prediction node is used to predict the property and behavior of the die casting material. The empirical model is used to correlate the microstructure parameters to the mechanical property of the material.

This work limits the interest to three nodes: calibration & validation, microstructure model, and material property and behavior prediction. Within this scope, UQ will be performed to increase the reliability of the proposed computational framework. There exists several major uncertainty factors that affect the quality of die casting products, and one of the major uncertainties that affects the mechanical behavior of die casting products is the microstructure. This inherent stochastic uncertainty of the microstructure propagates through the underlying physical behavior of materials and results in a significant performance deviation of the final product. Therefore, the necessity to characterize and quantify the

uncertainty in the microstructure has been raised for many years.

Quantitative metallography is the determination of characteristics of a microstructure by making quantitative measurements of metallographic images.[2] Measured quantities include the volume concentration of phases, grain size distribution, defect density and distribution, and surface area or volume ratio of the microconstituents. One of the commonly utilized microstructural information is the average grain size, i.e., its correlation with the fundamental mechanical properties of the material, such as stress-strain relationship, yield strength, hardness, and fatigue strength.[3]

Traditional grain size measurement methods fall into three categories: 1) comparison method, 2) planimetric method, and 3) intercept method. The comparison method measures the level of grain size by comparing the optical micrograph with the standard charts that display the sample micrograph and the corresponding average grain size.[4] It is the simplest method to measure the average grain size. However, this method can provide inaccurate measurement, and the applicability is only limited to the equiaxed and uniform grains. In the planimetric method, the grains are counted within a circle that is drawn on the micrograph with a user-defined area. The area of the circle divided by the number of grains within the circle gives the averaged grain size.[4] The accuracy of the planimetric method is also relatively low as the number of grains intersected by the circle is not a precise metric. In addition, the method can be easily biased when the number of grains inside the circle is not enough to provide statistically meaningful data. The intercept method measures the average grain size by drawing several straight lines over the micrograph and counting the number of grain boundaries intercepted by the lines.[5] The representative average grain size is the total length of drawn lines over the number of intercepted grains. Depending on the direction, length, and the number of lines determined by the operator, the measured grain size varies highly, resulting in an inconsistency in the measured data.

All measurement methods described above characterize the grain size distribution with a single averaged value. However, a recent study shows that the average grain size is not enough to describe the mechanical properties of a material since the grain size distribution can affect the mechanical strength of the material.[3c] To quantify the grain size distribution, a new technique called the point-sampled method was proposed. This technique randomly samples pixels and uses it as measurement locations.[6] At each location, the grain size is measured in four evenly spaced directions (0°, 45°, 90°, and 135°) following ASTM E1382 linear intercept length method.[5] This method is fully automated without any intervention by the operator which can typically result in some bias. However, it requires a relatively large number of sampling locations (more than 25% of the total number of pixels in the micrograph, which is often of the order of a million pixels) for statistical consistency, resulting in a high computational cost.

This work suggests a novel approach which is computationally efficient and accurate to characterize the grain size distribution. To do this, we improve the way to locate the measurement locations. Instead of using randomly selected points, we use the centroids of grains in the micrograph, so that the measurement accuracy is retained while using much fewer measurement locations. The centroid of each grain is obtained by the iterative voting algorithm,[7] which is one of the effective methods to locate the centroid of a randomly shaped geometry. From the found centroid locations, grain sizes are measured in four directions (0°, 45°, 90°, and 135°) following the ASTM standard.

To estabilish the accuracy of the iterative voting algorithm, synthetic micrographs with circular/elliptic grains are generated using user-defined sizes, orientations, and densities. The estimated grain size distribution from the iterative voting algorithm is compared with the given grain size distribution. Once the accuracy of the iterative voting algorithm is established, we apply it to the experimental micrographs taken from the literature. The estimated average grain

size from the iterative voting algorithm is compared with several other measurement methodologies, including the point-sampled method, manual measurement, and estimation from uniformly distributed points. In addition to the comparison of average grain size, we also compare the performance of the iterative voting algorithm with the point-sampled method in terms of computation efficiency and accuracy of measurement.

The measured microstructure information (e.g. grain size) can be correlated to the solidification results (e.g. temperature field, or temperature gradient field) by taking the microstructural evolution into consideration. Various approaches have been proposed to model the microstructural evolution: extensive review is given in the literature.[8] Among various theoretical and empirical relationships that have been proposed, the equiaxed grain growth model is taken into consideration in this study based on the experimental results. The solute concentration in the solidification process can be incorporated into the grain growth model, so that it can capture the accurate grain growth rate depending on the solute concentrations. In this study, the grain growth rate is further simplified by assuming that the grain growth rate is a function of the total undercooling and the restriction factor.[9]

The computational model for the grain growth predicts the grain size in the deterministic way: there is no stochastic parameters or probabilistic processes involved in the model. However, in the actual grain growth process, many stochastic process are involved during nucleation, grain growth direction, division, merging, etc. Therefore, we can expect the model discrepancy between the computational model and the experiment result. One way to systematically calibrate this discrepancy is defining the model discrepancy as the Gaussian process, proposed my Kennedy and O'Hagan.[10] In this framework, the measured grain size is the summation of the simulation result, model discrepancy term, and the measurement error. By feeding the simulation result and the corresponding experiment result, the amount of model discrepancy can be quantified. The quantified model discrepancies are considered as the

realizations of the Gaussian process, so that the parameter of Gaussian process can be estimated in the Bayesian framework.

The calibrated grain size information can be used to estimate the mechanical property of die cast parts, such as yield strength, toughness, Young's modulus, etc. The most common way to correlate the yield strength of material with the grain size is the use of Hall-Petch equation.[6b] In the equation, the yield strength of the material is the summation of starting stress for the dislocation movement and the term that is inversely proportional to the grain size. So, as the grain size decreases, the yield strength increases. However, the recent study shows that the grain size dispersion reduces the strength of the material.[3c] Therefore, we used the representative grain size that considers the mean of grain size dispersion as well as its standard deviation.

The aim of this chapter is the development of a novel computational framework that can help to understand the distribution of the mechanical property of die casting products. The proposed "input parameters-manufacturing process-product property" framework can connect the input parameters with final product quality through the reliable manufacturing process modeling. In order to accomplish this, the two methods will be presented: 1) the novel grain size measurement method, and 2) computational model calibration method. The proposed framework provides a general methodology that helps to calibration and validate the computational model that simulates the manufacturing processes with uncertainties.

5.2 Materials and methods

5.2.1 Image preparation

In this study, the optical micrograph is considered as a digital image that is defined as a finite set of digital values in 2D, which are called pixels. The (x, y) coordinate of each pixel corresponds to the location of the pixel, and the pixel value represents the grey scale intensity value or colors.[11] Before applying the iterative voting algorithm, two pre-processing steps are required to obtain an accurate grain size. First, the optical micrograph is converted into a binary image by thresholding. The thresholding differentiates the object of interest from the background by comparing each pixel intensity value as follows:

$$\begin{aligned} &If\ I(x,y) > \Gamma_b, I_B(x,y) = 1 \\ &otherwise, I_B(x,y) = 0 \end{aligned} \tag{5.1}$$

where $I(x, y)$ is the pixel intensity at the location (x, y) in the image, Γ_b is the intensity thresholding value, and I_B is the binary representation of the image. If the pixel intensity $I(x, y)$ is higher than Γ_b, $I_B(x, y)$ =1 is assigned, else $I_B(x, y)$ equals to 0. Because the pixel intensities of the object and the background are often fairly consistent with their respective values, the thresholding value can be determined by the pixel intensity histogram of the image.[12] If there exists a smooth change in the background intensities such as spatially varying illuminations over the image, the adaptive thresholding technique can be applied to obtain an accurate binary representation of the image.[13] Second, small holes or speckles inside the grains are removed from the image. These small holes or speckles are often generated by noises in the optical measurement devices or digitization process, reducing the accuracy of measurement. Because these small features are usually one order of magnitude smaller than

the grain size, they are deleted based on their size and circularity.

5.2.2 Iterative voting algorithm (IVA)

In the point-sampled linear intercept method, the measurement locations are not closely related to the feature of the given micrograph. By relating the measurement locations with the feature of micrograph, i.e., centroid, the grain size can be measured accurately even if a limited number of measurement locations are used. One of the effective methods to locate the centroid of randomly shaped geometry is using the iterative voting algorithm.[7] In this study, the IVA is employed to locate the centroids of grains, so that the grain size measurement is performed efficiently while retaining the accuracy of the measurement.

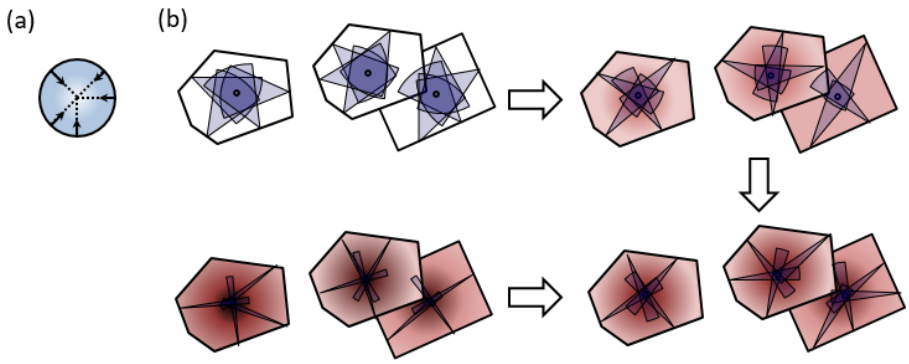

Figure 5.2 (a) Locating the centroid using the radial symmetry when the grain is circular. (b) Locating the centroid using the iterative voting algorithm. Sequential procedures display how to locate the centroids of randomly shaped grains.

IVA is a method to detect the centroid location of objects in the image, such as biological cells, granular structures, particles, that have inexact radial symmetry. For a particle with radial symmetry, the centroid location can be easily found by drawing lines from the

boundary of the particle along the radial direction as shown in Figure 5.2 (a). However, in randomly shaped particles, such as grains in the microstructure, it is not easy to locate the centroid using the radial lines. Instead of lines, IVA introduces the voting intensity map and a series of voting kernels. The voting intensity map is initially of the same size as the original image with zeros. The centroid location will have a high local voting intensity than the neighboring pixels and will be used for locating the centroid. Instead of radial lines, IVA uses a series of kernels that vote iteratively along the radial direction. This kernel is determined by the shape of particles, for example, a circular sector starting at the boundary pixel of the particle and defined by the min/max radius and the angle.

Because the intensity gradient is high at the grain boundaries, we can locate the pixels at the grain boundaries by using thresholding of the intensity gradients. At each pixel in the grain boundaries, the initial voting direction, $\theta_0(x, y)$, is determined using the intensity gradient and will be updated in every iteration. Along the initial voting direction, the voting intensity is updated by summation of pixel intensity inside of the voting kernel. After processing all the pixels in the grain boundaries, the pixels near the center of grains have higher voting intensities compared with the pixels away from the center (see Figure 5.2 (b)). After the voting intensity map is updated, the voting direction is also updated by the value that maximizes the summation of all voting intensities in the voting kernel. By repeating this process until n reaches to N, IVA can generate the voting intensity map that has highly localized intensities near the center of each grain. Lastly, IVA can locate the centroid of each grain by thresholding the voting intensities.

IVA can locate the centroid even in the none-closed grain boundaries, micrographs with high noise, large variations in scales and shapes which are usually hard to find the centroids.[7] Various parameters are needed to be defined in the IVA: intensity thresholding

value for determining the centroid location (Γ_c), the radius of the circular sector ($r_{\max}$), and a series of voting angles for the circular sector $\Delta = \{(\Delta_i) \mid i = 0,..., \mathrm{N}, \Delta_0 > \Delta_1 >,...,> \Delta_N\}$. The series of voting angles are defined in a reducing order so that the voting area becomes focused as iteration proceeds. The pseudo-code for the IVA is as follows, and more extensive details on IVA are given in Ref. [7]:

Algorithm 5.1 Iterative voting algorithm (IVA)

// Initialization

- Preprocessing of the micrograph
- Set intensity thresholding value(Γ_c), and voting area parameters ($r_{\max}, \Delta$)
- Initialize voting direction:

  For $(x, y) \in B$ *where* $B = \{(x, y) \mid \|\nabla I_B(x, y)\| \neq 0\}$

$$\theta_0(x, y) = -\frac{\nabla I(x, y)}{\|\nabla I(x, y)\|}$$

- Initialize voting intensity $V(x, y) = 0$ *for all* (x, y)

// Update voting intensity

- *For* $(x, y) \in S$ *where* $S = \{(x, y) \mid I_B(x, y) > 0\}$

$$V(x, y) = V(x, y) + \sum_{(u,v) \in A(x,y;r_{\max},\Delta_n)} I(u, v)$$

where $A(x, y; r_{\max}, \Delta_n) = \{(x \pm r\cos\phi, y \pm r\sin\phi) \mid \mathrm{r} \leq \mathrm{r}_{\max}$ *and* $\theta_n - \Delta_n \leq \phi \leq \theta_n + \Delta_n\}$

// Update voting direction

- *For* $(x, y) \in B$

$$(u^*, v^*) = \arg \max_{(u,v) \in A(x,y;r_{\max},\Delta_n)} V(u, v)$$

$$\theta_n(x, y) = \frac{(u^* - x, v^* - y)}{\sqrt{(u^* - x)^2 + (v^* - y)^2}}$$

// Refine the angle: $\Delta_n \rightarrow \Delta_{n+1}$

// Repeat the process from updating voting intensity until *n* reaches to N

// Determine the centroid location: $C = \{(x, y) \mid \mathrm{V}(x, y) > \Gamma_c\}$

5.2.3 Centroid merging algorithm

The accuracy of IVA also depends on the convexity and local curvature of grain boundaries. When the local curvature is small at the certain locations, there exists a localized area where its voting intensity becomes relatively higher than its neighbors. In this case, IVA produces multiple centroid locations within one grain. Therefore, modifications are needed to the algorithm so that the local centroids within one grain can be merged. The following pseudo-code shows the brief idea of how multiple centroids can be merged.

Algorithm 5.2 Centroid merging algorithm

// *For i^{th} centroid*,

- Find the nearest p centroids.
- Draw a line between the i^{th} centroid and each of p centroids.
- Calculate ∇I along the lines.
  // *For the j^{th} centroid in p centroids*
  - If ∇I on the line between the *i^{th} and j^{th} centroids* has a sharp peak, this means the line passes the grain boundary: do not keep the index j.
  - If ∇I does not have a sharp peak, keep the index j
  - *Repeat until j equals p*
- merge centroids: merged centroid location is calculated by:

$$L_x = \frac{V_1 x_1 + V_2 x_2 + ... + V_k x_k}{V_1 + V_2 + ... + V_k}, L_y = \frac{V_1 y_1 + V_2 y_2 + ... + V_k y_k}{V_1 + V_2 + ... + V_k}$$

  where L_x, L_y are the x and y coordinate of the merged centroid, respectively, and $V_1, V_2, ..., V_k$ are the voting intensities of k centroids.

The merged centroid location is an averaged X and Y coordinate of multiple centroid locations weighted by its voting intensity. Since the voting intensity is proportional to the number of boundary pixels that correspond to the centroid, the weighted average gives a better estimate of the true centroid than the simple averaging.

5.2.4 Linear intercept method

The linear intercept method measures the grain size in eight evenly spaced directions (0°, 45°, 90°, 135°, 26°, 63°, 117° and 154°). The first four angles are chosen from the ASTM E1382 linear intercept length method [5], and the remaining angles are chosen for additional directional consideration. The measurement locations are the centroid locations obtained from the IVA and merging algorithm. The eight values from all measurement directions are averaged to represent the grain size of the micrograph.

5.2.5 Grain growth model

To correlate the microstructure information (e.g. grain size) with the solidification results (e.g. temperature field, or temperature gradient field), the grain growth model is required in the framework. The equiaxed grain growth are assumed based on two reasons: 1) the equiaxed grain shape observed in the experiment, and 2) instant solidification time (< 3 seconds) in the experiment. The spherical crystal growth model[14] is used to model the equiaxed grain growth during the solidification process.

The basic assumption of the spherical crystal growth model is that the curvature and the solutal undercoolings are only significant amount of undercooling in the single crystal growth.[14] Then, the total amount of undercooling (ΔT) of a spherical crystal of radius (r) is:

$$\Delta T = \Delta T_S + \Delta T_C = m(\mathrm{C}_0 - C_{IL}) + \frac{2\sigma}{\Delta S_V r} \tag{5.2}$$

where ΔT_c and ΔT_s are the curvature undercooling and the solutal undercooling, respectively.

m is the liquid slope and the C_0 and C_{IL} are the initial solute concentration in the liquid metal and the solute concentration in the melt at the liquid-solid interface, respectively. σ is the liquid-solid interfacial energy and ΔS_v is the entropy of fusion per unit volume. In an isothermal melt, the radius, r, of a growing spherical crystal is:

$$r = \lambda_S (D_S t)^{1/2}$$
$$\lambda_S = \left(\frac{-S}{2\pi^{1/2}} \right) + \left(\frac{S^2}{4\pi} - S \right)^{1/2} \quad (5.3)$$

where D_s is the diffusion coefficient of liquid metal, and the λ_s is the growth coefficient that is defined by *S*. For the alloys that satisfy $|S|<0.3$, the invariant approximation can be commonly applied to the model.[15] In addition, when the effective nucleant (~ 2μm) is present in the aluminum alloy, this expression can be further simplified as follows: [9]

$$S = \frac{2(C_{IL} - C_0)}{(C_{IS} - C_{IL})} \approx \frac{-2\Delta T_n}{Q} \quad (5.4)$$

where ΔT_n is the amount of undercooling when the nucleant is present, and Q is the restriction factor for grain growth. The values for the ΔT_n and Q can be found in the literatures.[9, 16]

5.2.6 Calibration model for the grain size map

The grain growth model correlates the grain size and distribution with the results from the solidification model, such as temperature and temperature gradient. The models that we used for grain growth and solidification are implemented in deterministic way: there are no stochastic parameters involved in the model. Therefore, there exists inevitable discrepancy between the calculated grain size and the measured grain size from the experiment. This discrepancy in the grain size and distribution comes from multiple reasons: 1) stochastic nucleation process, 2) stochastic growth process (e.g. direction, division, and merging), 3) natural convection of grains during solidification process, and so on.

The Gaussian process model can be used to represent the model discrepancy caused by the stochastic nature of grain growth, following the Kennedy and O'Hagan framework.[10] In this framework, the measured grain size is the summation of the simulation result (model), model discrepancy term, and the measurement error:

$$r_{\exp}(\mathrm{x}_i) = r_{sim}(\mathrm{x}_i;\Omega) + \delta(\mathrm{x}_i) + e_i \tag{5.5}$$

where $r_{\exp}(\mathrm{x}_i)$ and $r_{sim}(\mathrm{x}_i;\Omega)$ are the experiment result and simulation result at i$^{\text{th}}$ location, x_i. Ω is the parameters in simulation. $\delta(\mathrm{x}_i)$ is the simulation bias term at x_i that is modeled as a stationary Gaussian process. e_i is the measurement error term (e.g. error bounds that can be caused by choice of parameters in the image processing). Therefore, the stochasticity in grain growth are merged into one stochastic term in calibration process, which is $\delta(\mathrm{x}_i)$ in this framework.

2D Gaussian process model is used for the model discrepancy term because the thickness of the sample is small so that the grain size and distribution is homogeneous along the thickness direction. Similar to the modeling of spatial uncertainty in Chapter 4, the Bayesian approach can be used to estimate the parameters in the Gaussian process. The proposed 2D Gaussian process model is as follows:

$$\begin{aligned} &\delta \mid M, C \sim GP(M, C) \\ &M : x, a, b, c, d, e, f \rightarrow ax^2 + bx + cy^2 + dx + exy + f \\ &C : x, x', l \rightarrow \exp\left(-\frac{(x - x')^2}{2\theta^2} \right) \end{aligned} \tag{5.6}$$

where the M and C are the mean and covariance functions, respectively. a through f are the coefficients of the mean function and l is the correlation length of the covariance function. The mean function is modeled as the second order polynomial function under the assumption that the discrepancy changes smoothly over the domain. The covariance function is modeled as a squared exponential function, assuming the correlation of spatial stochasticity decreases monotonically as the distance between two locations increases. This Gaussian process model helps to take the stochasticity of grain growth procedure into consideration.

5.2.7 Correlation between the grain size and the yield strength

The grain size information can be used to estimate the mechanical property of die cast parts, such as yield strength through Hall-Petch equation.[6b] The traditional Hall-Petch equation considers the yield strength as a function of averaged grain size.

$$\sigma_y = \sigma_0 + kd^{-1/2} \tag{5.7}$$

where σ_0 and σ_y are the starting stress for the dislocation movement and the yield strength of the material, respectively. k is the strengthening coefficient. d is the grain size.

However, the recent study shows that the grain size dispersion reduces the strength of the die cast materials.[3c] One of common ways to include the effect from the grain size dispersion on the yield strength is considering the range of grain size.[6b] The following empirical relation shows how the grain size dispersion can affect the yield strength of the material.

$$\sigma_y = \sigma_0 + \frac{k}{\sqrt{d}}\left(1 + f\frac{\Delta d}{d}\right)$$
$$\frac{\Delta d}{d} = \frac{d_{99\%} - d_{1\%}}{d} \tag{5.8}$$

Δd is the average grain size and the grain size dispersion, which is defined as the difference between the maximum grain size taken as 99 % probability level grain size ($d_{99\%}$) and the minimum grain size taken as 1 % probability level grain size ($d_{1\%}$). Even though this expression is widely used in the literature, the definition of the grain size dispersion that covers the range from the minimum and the maximum values of grain size cannot specify the details of grain size dispersion. Therefore, we consider the representative grain size that can characterize the yield strength of die cast parts that has a certain grain size dispersion.[17] The representative grain size is defined as a function of mean and standard deviation of grain size dispersion:

$$D_R = \exp\left(M + \frac{11}{4} S^2 \right) \tag{5.9}$$

where M and S are the mean and standard deviation of grain size dispersion. Therefore, the Hall-Petch equation can be updated with the representative grain size, considering the effect from the grain size dispersion.

$$\sigma_y = \sigma_0 + k D_R^{-1/2} \tag{5.10}$$

5.3 Results and discussion

5.3.1 Synthetic micrographs: circular and elliptic grains

We present two test examples to illustrate the accuracy of the iterative voting algorithm. The two test examples are synthetic micrographs with circular and elliptic grains, which are generated by user-defined sizes, orientations, and densities.[18] The micrograph is in a binary format where the grains are in white, and the background is in black. The sizes of the two synthetic micrographs are 512x512 pixels. Figure 5.3 (a) shows the micrograph with circular grains and the centroid locations obtained by the IVA. The centroid is located in each grain, and the accuracy of the located centroid is estimated by looking at the measured grain size. Figure 5.3 (b) displays two histograms of grain size that are measured by the IVA and the point-sampled intercept method. The X-axis is the grain size in each bin, and the normalized count is displayed along the Y-axis to have the area under the histogram equal to 1. The diameter of the grain that is used for generating the synthetic micrograph is 34 pixels and shown as dotted line in Figure 5.3 (b). The mean values of the grain size measured by the IVA are 33.38 pixels within the 1-pixel error bound. However, the point-sampled intercept method gives 28.49 pixels. In addition to the comparison of the mean of grain size, the grain size distribution should be estimated accurately when the effect from grain size dispersion is considered. A recent study showed that the grain size dispersion, as well as the mean grain size, influences the mechanical properties.[3c] While most of the grain size estimation by IVA is near the given grain size, the grain size distribution by the point-sampled intercept method has a big spread due to its random selection of measurement location.

The same result is observed when the synthetic micrograph with elliptic grains is tested. The user-defined major and minor axis lengths of the elliptic grain are 42 pixels and 22 pixels, respectively. Figure 5.3 (c) shows the synthetic micrograph with local centroids found by IVA. Due to the small local curvature observed in ellipses, IVA finds two local centroids in each

grain as shown in Figure 5.3 (c). The centroid merging algorithm can estimate an accurate centroid location of all the elliptic grains by using the local centroids (see Figure 5.3 (d)). As the orientation of elliptic grains is randomly chosen, the expected grain size distribution is relatively uniform over the range from 22 pixels to 44 pixels, which is displayed in dotted lines. As shown in Figure 5.3 (e), 95 % of all the measurements are located within the range of 22 pixels to 42 pixels. However, the point-sampled intercept method produces a widely distributed grain sizes over the range from 10 pixels to 45 pixels, and only 72 % of measurements are correctly located within the range of 22 to 42 pixels.

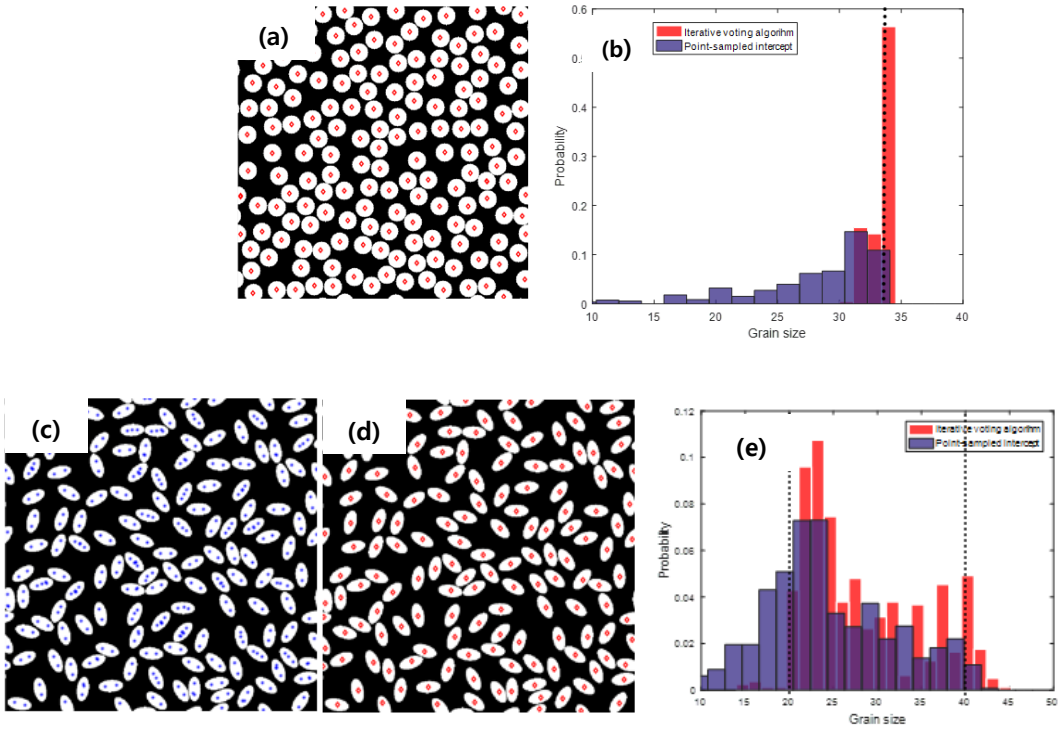

Figure 5.3 (a) Synthetic micrograph of circular grains and located centroids from IVA (red dots), (b) Estimated grain size distribution from point-sampled method (blue) and IVA (red), (c) Synthetic micrograph of elliptic grains and located centroids from IVA (blue dots), (d) Merged centroids from centroid merging algorithm (red dots), (e) Estimated grain size distribution from point-sampled method (blue) and IVA (red)

5.3.2 Experimental micrographs from the literature

To further understand the accuracy and computational efficiency of the IVA, we apply our algorithm to experimental micrographs. Six experimental micrographs are taken from the literature.[19] These micrographs are chosen from the literature as each micrograph has different average grain size, and the manually measured mean and standard deviation of grain size are given in the literature. The binary representation of the experimental micrographs after the pre-processing steps are shown in Figure 5.4 (a-f). The grains are shown in white, and the rest is shown in black. The centroids found by IVA and the merging algorithm are displayed as red dots on top of each binary image. The linear intercept method is used to measure the grain size at the located centroids.

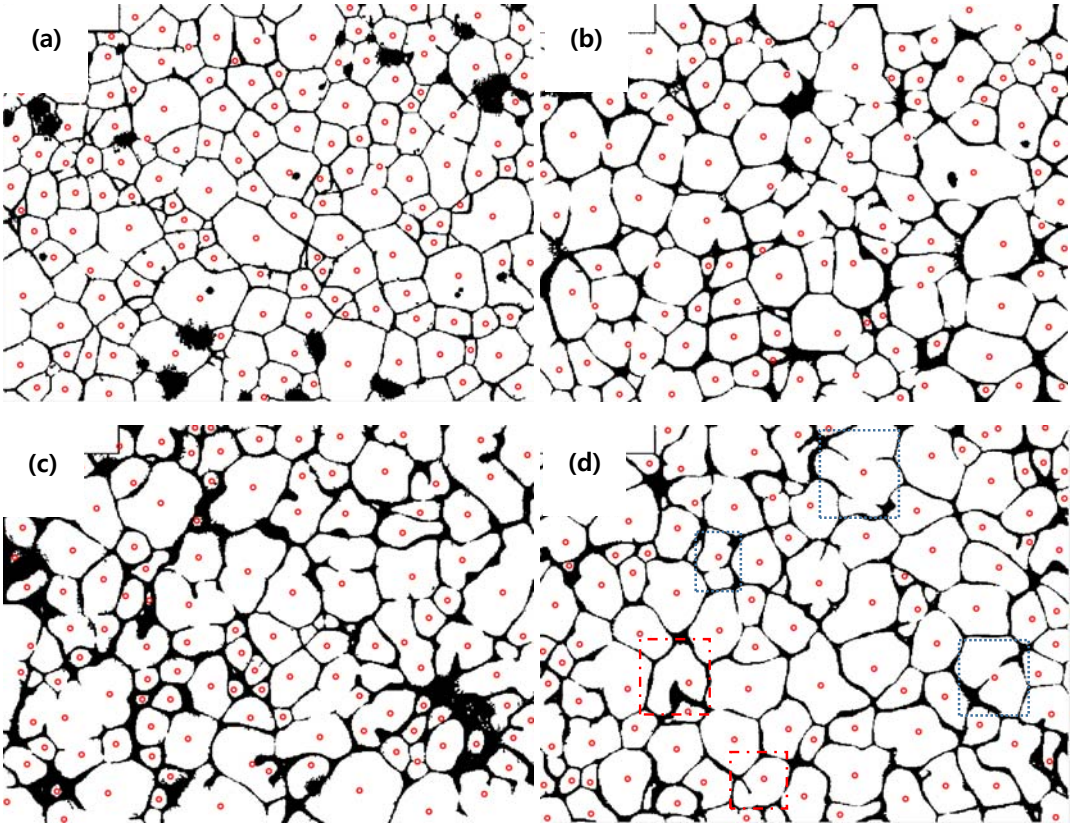

Figure 5.4 (cont.)

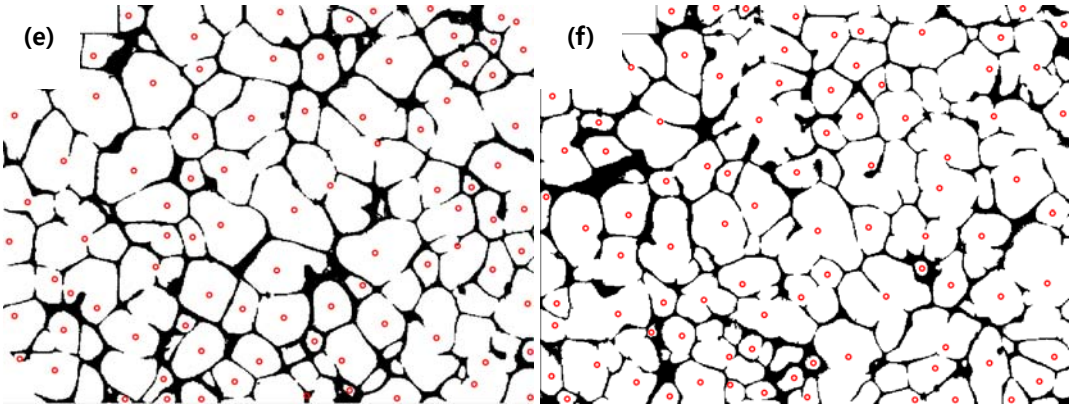

Figure 5.4 The binary representation of experimental micrographs after the pre-processing steps and located centroids from IVA and centroid merging algorithm.

A comparison of the grain size measured with the four different methods including the IVA is shown in Figure 5.5. The four different methods are: 1) IVA and linear intercept method (circle), 2) point-sampled linear intercept method (inverted triangle), 3) manually measured values from the literature[19] (diamond), and 4) linear intercept method with uniformly distributed measurement locations (rectangle). In the uniformly distributed measurement locations, the number of measurement locations is the same as the number of centroids found by IVA, but they are uniformly distributed over the image. The X-axis is the experimental micrograph index ranging from 1 to 6 corresponding to Figure 5.4 (a-f), respectively. Y-axis denotes for the measured grain size, and the error bars are taken from the standard deviation values in the literature.[19]

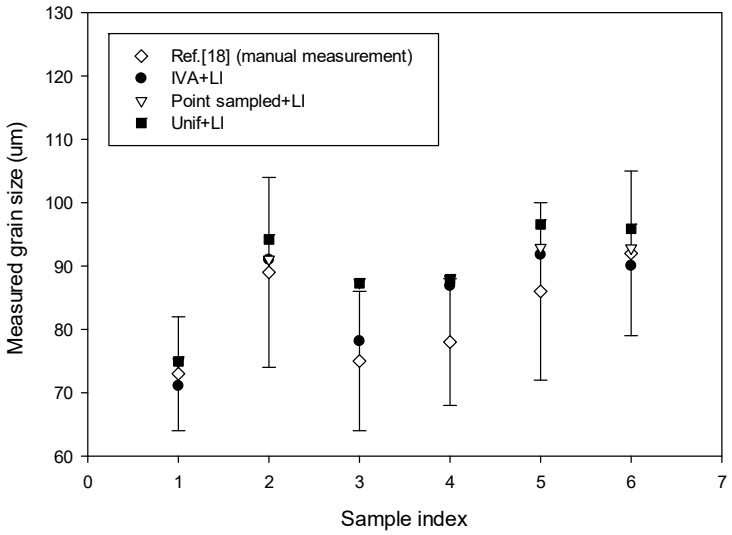

Figure 5.5 A comparison of the grain size measured with the 4 different methods: 1) IVA and linear intercept method (circle), 2) point-sampled linear intercept method (inverted triangle), 3) manually measured values from the literature[19] (diamond), and 4) linear intercept method with uniformly distributed measurement locations (rectangle).

The measured grain sizes from the IVA are within the standard deviation in all the examples. This implies that the IVA provides consistent results with the manual measurements. The largest deviation between the manual measurement and the IVA is less than 12% of the measured mean grain size, which is reasonable as the average standard deviation in 7 examples is around 15% of measured mean grain size. In addition there can be errors in the manual measurement due to the operator's decisions regarding measurement locations, directions of measurement, line lengths of measurement, etc.

We also compared the result from the IVA with the result from the point-sampled intercept method. From the central limit theorem,[20] increasing the sampling density makes the sampled grain size distribution converges to the true grain size distribution. In this study, we sample 40% of the total number of pixels for the consistency of measurement as recommended

in the literature.[6] As shown in Figure 5.4, the measured grain size by the IVA is consistent with the point-sampled intercept method in all example micrographs, which is close to the true grain size distribution. From this we can conclude that the IVA can measure the grain size that is consistent with the manual measurement as well as the point-sampled intercept method.

The effectiveness of the IVA is more distinctive when its results are compared with the results from uniformly distributed measurements. The grain size measured by the same number of measurement locations as the IVA but uniformly distributed measurement locations shows a significant deviations from the point-sampled linear intercept method as well as the manual measurement. The difference between the results from the uniformly distributed measurement locations and the IVA becomes even more significant when the micrographs with inhomogeneous grain size distribution are considered.

To further evaluate the difference between the IVA and the other methods, the smallest and largest deviation between the estimated and given average grain size are compared to each other. Those cases are shown in Figure 5.4 (a) and (d), respectively. The possible reasons for estimation accuracy are: 1) clear grain boundary, 2) convexity of grain shape, 3) uniformity of grain size.

First, clear grain boundaries in the micrograph increase the accuracy of the iterative voting algorithm, resulting in an accurate measurement of grain size. The open grain boundary often ends up with an inaccurate centroid location as shown in the boxed areas (blue dotted lines) in Figure 5.4 (d). In microstructures, several grains are often merged, resulting in blurred grain boundaries due to the light scattering at the edge of the grains. There are two possible ways to get clear grain boundaries: 1) using the level set algorithm, and 2) using the electron backscatter diffraction (EBSD). The level set algorithm is an image segmentation technique that differentiates the grains from the background by utilizing the internal properties of the

image (pixel intensities) and an external property, such as contour length regularization.[21] By applying the level set algorithm with a repulsive force that prevents the merging between neighboring grain boundaries, it can guarantee closed grain boundaries.[22] EBSD is a microstructural characterization technique using which the structure, crystal orientation, and phase densities can be measured. This technique helps in providing clear grain boundaries, which can result in better accuracy of the IVA. This work does not consider these options because the purpose of this work is to introduce the measurement framework using the iterative voting algorithm that can increase the computational efficiency while preserving the measurement accuracy. However, these options can be incorporated with the IVA framework to increase the accuracy of the grain size measurement.

Second, the convexity of the grain shape is related to the accuracy of the iterative voting algorithm. In the case of convex grains, the centroid can be found accurately by the iterative voting algorithm. The non-convexity typically arises from the non-clear grain boundaries or due to the nature of the grain growth. When the grain has a non-convex shape, the IVA ends up with several local points. This work proposes the merging algorithm which can merge multiple points that are found from the IVA, but it is not a perfect solution for all randomly shaped grains. The boxed areas (red dash lines) in Figure 3d show several locations that are falsely found centroids due to the non-convexity of the grains. This inaccuracy in the IVA can reduce the accuracy of the grain size measurement. A general algorithm, such as the multiscale surface projection, can accurately locate the centroid of randomly shaped objects in space, and the details are described in the literature.[23]

Finally, the uniformity of the grain size can affect the match between the measured grain size by the IVA and the average grain size that is given in the literature. The average grain size in the literature is the manually measured grain size, so it depends heavily on the operator's decision of the measurement location. The dependency on the measured grain size

on the measurement location becomes more significant when the grain size distribution is non-uniform over the micrograph. Therefore, the micrograph with the non-uniform grain size, such as Figure 5.4 (d), is prone to errors when the manual measurement is used. On the other hand, the results from IVA and the point-sampled intercept method, which estimate the average grain size from the grain size dispersion, are consistent with each other. Thus, when the grain size is not uniform in the micrograph, it is highly recommended to use the measurement methods, such as the IVA as well as the point-sampled intercept method.

The accuracy and computational efficiency of the IVA algorithm is compared with the point-sampled intercept method. The solid line in Figure 5.4 (a) shows the variation of the normalized average grain size when the number of sampled points is varied. The micrograph used for this is the 1st sample case shown in Figure 5.6. The X-axis is the number of sampled points divided by the total number of pixels in the image. Y-axis is the average measured grain size divided by the converged grain size in the point sampled intercept method. For each data point, the grain size is measured six times separately with different sampled points, so that the average is marked as the point and the standard deviation is displayed as the error bar.

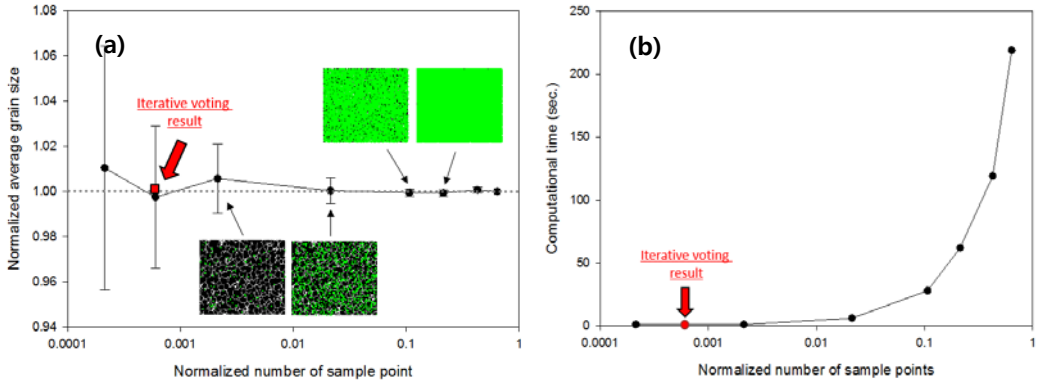

Figure 5.6 (a) Variation of the normalized average grain size when the number of sampled p oints increases. The normalizing value for the X-axis and the Y-axis are the total number of p ixels in the micrograph and the grain size given in the literature.[19] The subplots show the den sity of the sampled points on top of the micrograph. The red dot shows the performance of IV A. (b) Computational time increases exponentially when the number of sampled-points incre ases. The red dot shows the computational time required in IVA.

As the number of sampled-points increases, the average value of the grain size converges to the mean of the total grain size distribution and the standard deviation decreases. The red dot in Figure 5.6 (a) shows the result from the IVA. The measured grain size shows a good match with the estimated mean grain size from the point-sampled intercept method (within 0.1 %) while it only uses 0.07 % of the total number of pixels.

The advantage of IVA is more distinctive when the computational efficiency of two algorithms is compared. Figure 5.6 (b) shows the change in computational time as the number of sampled-points increases. The computational time increases as the number of sampled-points increases. We note that it takes less than 1 second to measure the grain size with IVA and IVA at least 30 times faster than the point-sampled intercept method for the same level of accuracy. There are currently efforts to measure the grain size distribution of multiple

micrographs that are obtained sequentially from layer-by-layer sectioning and polishing.[24] For examples like these, IVA can be effective in determining the grain size distribution in a computationally efficient manner.

5.3.3 Experimental micrographs from experimental specimens

Experiments are carried out by the die casting company to produce a model specimen chosen from real-life die casting. The tub-shaped geometry in Figure 5.7 (a) show the model specimen that is used in this study. Figure 5.7 (b) and (c) show the locations where the micrographs are taken. The tub geometry are sectioned and polished as shown in the figure. On the polished face of each section, micrographs are obtained at 8~10 different locations (corresponding numbers are shown in the figure).

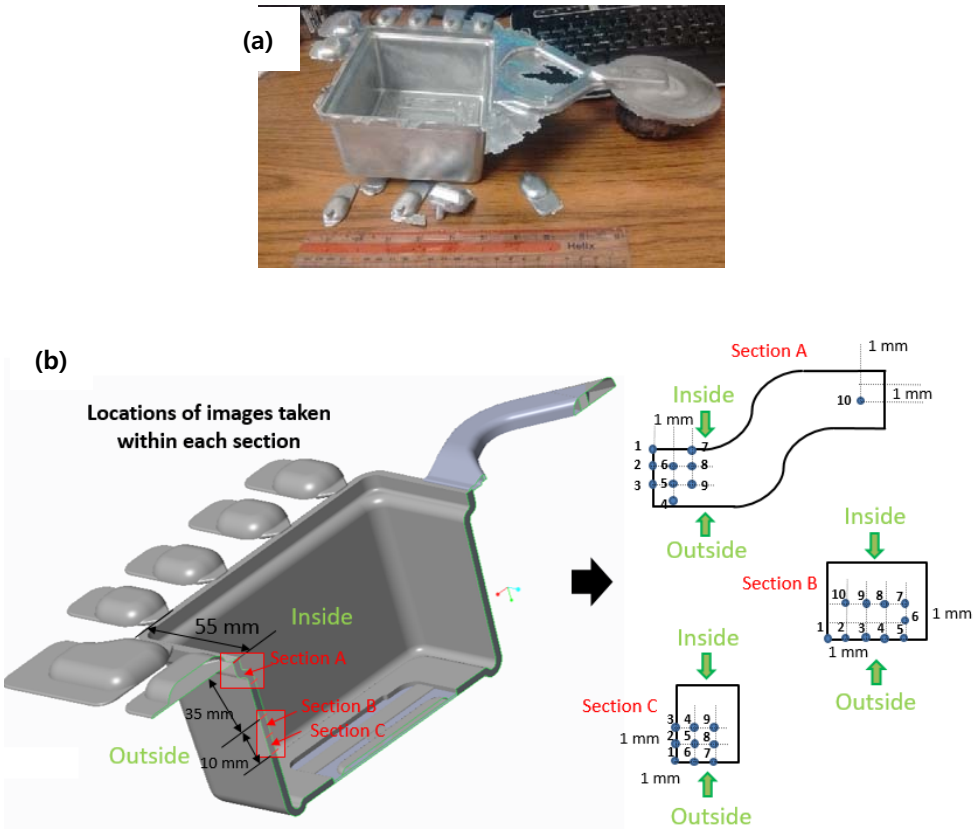

Figure 5.7 (cont.)

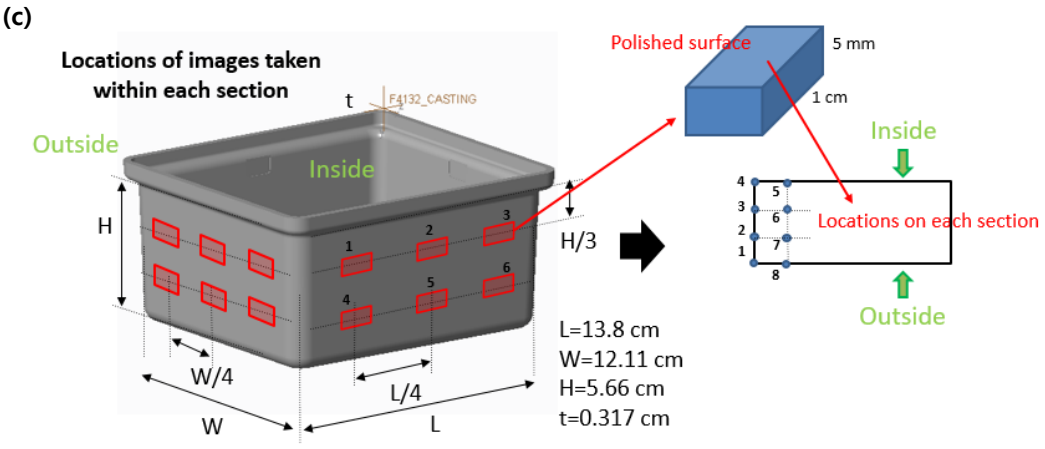

Figure 5.7 (a) The tub-shaped specimen for validation and calibration. (b) Vertical sectionin g of the specimen and locations where the micrographs are taken. (c) Horizontal sectioning o f the specimen and locations where the micrographs are taken.

More than 120 micrographs are obtained from the vertical and horizontal sectioning. 8 experimental micrographs in the horizontal sectioning are shown in Figure 5.8 as an example. Most of the grains have similar size distribution over all micrographs.

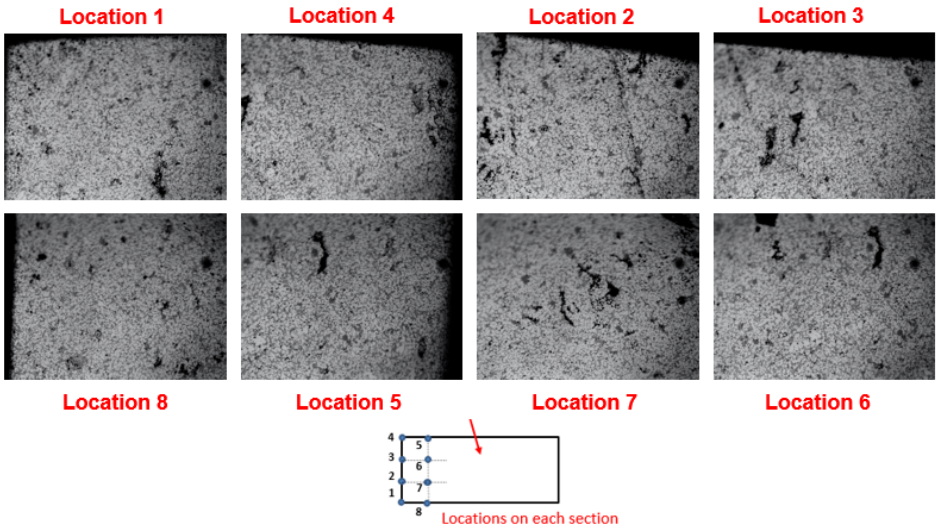

Figure 5.8 8 micrographs from horizontal sectioning at section 7. 8 different locations are m arked as location number in red and corresponding locations in the section are displayed at th e bottom.

The experimental micrographs are recognized as an image, so that the well-developed image processing techniques are used to extract microstructure information. The random sampling with the linear intercept method[6a] is used to characterize the grain size. The linear intercept method measures the grain size in four evenly spaced directions (0°, 45°, 90°, and 135°) following ASTM E1382 linear intercept method.[4] Two of the obtained grain size distribution are shown in Figure 5.9. The upper histograms show the grain size distribution as a bar chart and the fitted gamma and lognormal distribution. The lower histograms display log of upper two histogram.

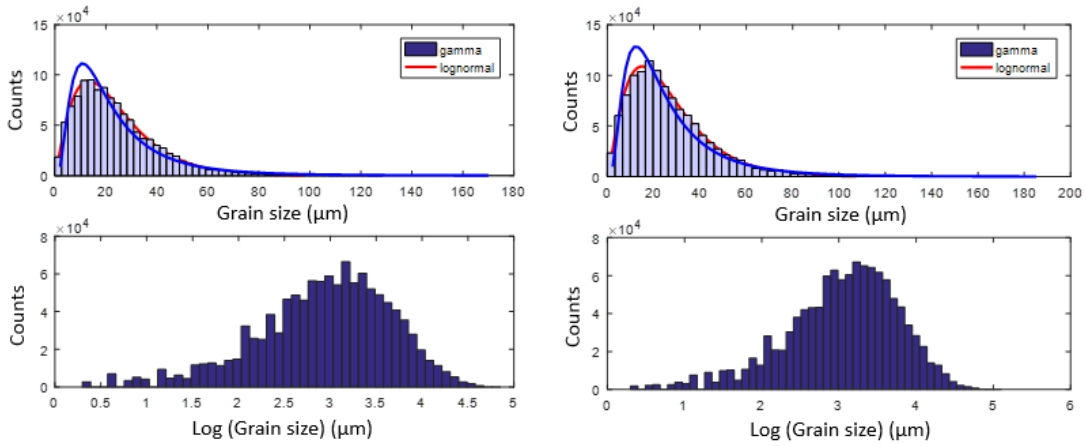

Figure 5.9 Extracted grain size distribution (upper histograms) and its log distribution (lower histograms) that are obtained from the experimental micrographs. The red and blue curves s how the lognormal and gamma distributions that are fitted with the obtained grain size distrib ution.

The mean and standard deviation of the fitted lognormal distributions are shown in Figure 5.10. The legend shows the section numbers that correspond to the location in the tub geometry. The x-axis is the sample location where the micrograph are taken in each section, and the y-axis is the mean and standard deviation of the fitted lognormal distribution. As

shown in the figure, there exists no significant difference in the mean and standard deviation values between the locations.

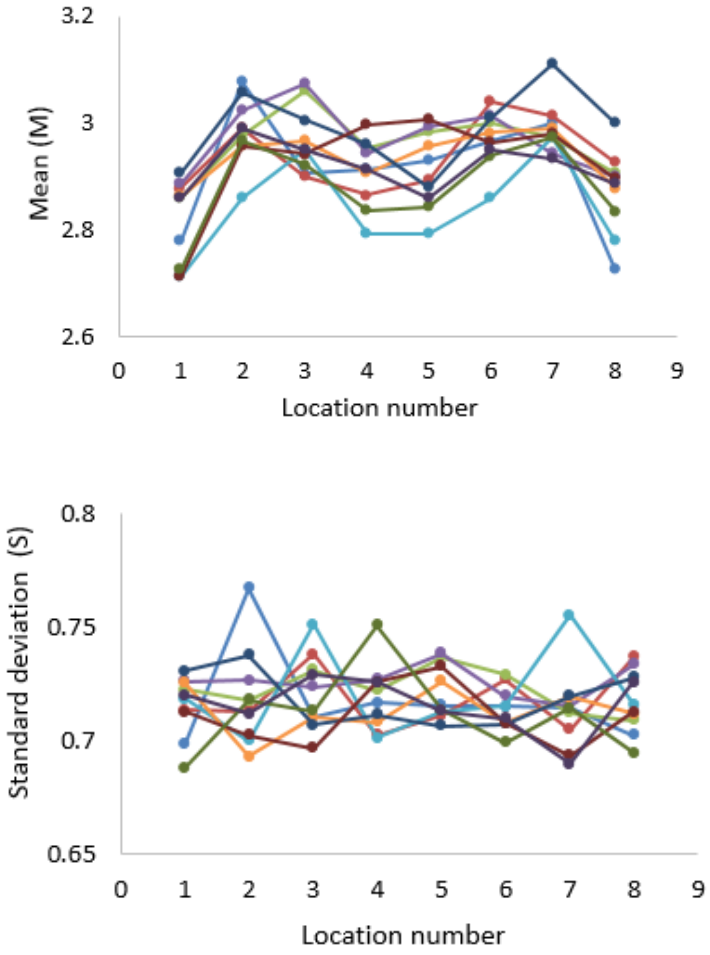

Figure 5.10 The mean and standard deviation of the fitted lognormal distributions that are ob tained from the experimental micrographs. X-axis shows the location number and Y-axes sho w the mean and standard deviation of fitted lognormal distribution of grain size. Different co lor of data trend stands for the different section number.

This measured grain size information of all micrographs can be used to estimate the mechanical property of die cast parts, such as yield strength, through Hall-Petch equation.[6b] However, the recent study shows that the grain size dispersion reduces the strength of the die cast materials.[3c] Therefore, the representative grain size that can characterize the yield strength of die cast parts that has a certain grain size dispersion[17] is calculated. Figure 5.11 shows the representative grain size calculated from the mean and standard deviation of grain size distribution measured in the experiment. Again, the representative grain size does not show the statistically significant change when the location of micrographs is changed.

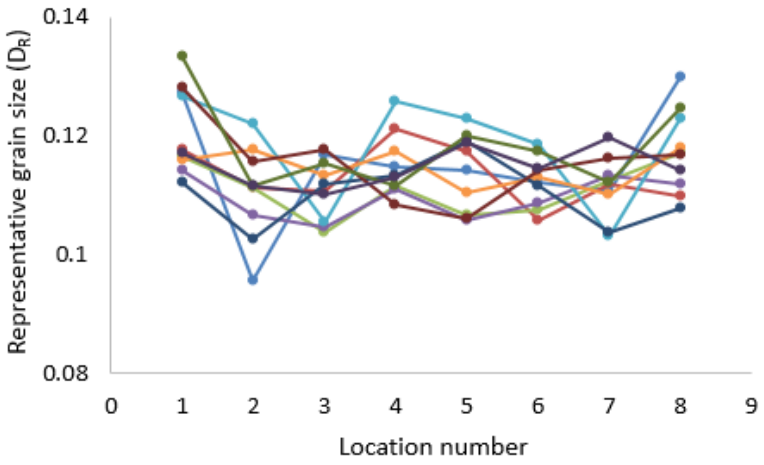

Figure 5.11 The representative grain size. X-axis and Y-axis shows the location an represent ative grain size, respectively. Different color of data trend stands for the different section nu mber.

5.3.4 Calibration of model discrepancy using 2D Gaussian process model

Before the 2D Gaussian process model is directly applied to quantify the model discrepancy term, we present a test problem to illustrate and verify the Gaussian process modeling framework. We verify our methodology by following procedures: 1) Generate the realizations from Gaussian process model with the mean and covariance functions that have the given parameters. 2) Sample the realizations and use it as the input for parameter estimation. 3) Compare the estimated parameters with the given parameters for verification.

The 2D Gaussian process within the domain with known parameters is as follows:

$$\begin{aligned} &\delta \mid M, C \sim GP(M, C) \\ &M \rightarrow -5x^2 + 0x - 3y^2 + 0y + 5 \\ &C : x, x', l \rightarrow \exp\left(-\frac{(x - x')^2}{2 * 0.2^2} \right) \end{aligned} \tag{5.11}$$

where M and C are the mean and covariance functions of the Gaussian process, δ. x and y are defined in the domain, $x, y \in [-1,1]$. The mean function is modeled as the second order polynomial function under the assumption that the discrepancy changes smoothly over the domain. The coefficients of polynomial are carefully chosen to have the negative values at the edge and the positive values at the center. Physically, the grains that are instantly formed near the edge of the domain expect to have smaller size than the grain size predicted from the diffusion limited growth model. In addition, the diffusion limited model expects to under-predict the actual grain size at the center location because the validity of diffusion limited is questionable at the center location. The covariance function is assumed as the squared exponential function because the correlation length during the grain growth is very

limited near the nucleation site and the effect decreases exponentially. But, there is still flexibility to increase or decrease the correlation region by changing the correlation length, *l*.

5000 realizations extracted from the given Gaussian process model are used as the input for estimation, where we try to reconstruct the parameters of the actual stochastic process from which data originated. Figure 5.12 shows the 9 realizations from the given Gaussian process model.

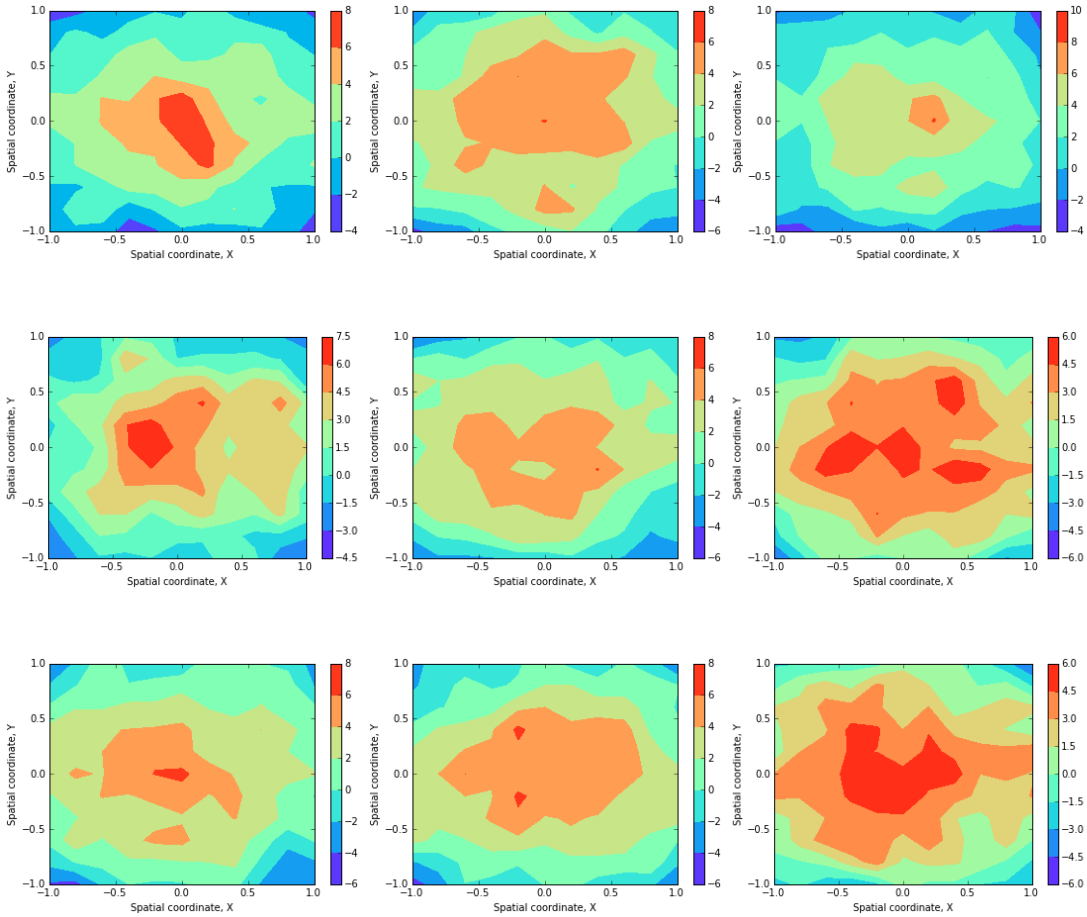

Figure 5.12 The 9 realizations from the 2D Gaussian process given in Equation (5.11). The g iven parameters are: *a=-5, b=0, c=-3, d=0, e=0, f=5, θ=0.2*.

The Gaussian process with general form of mean and covariance functions (Equation (5.6)) as well as the probability density functions (PDFs) are assigned for the unknown parameters:

$$\begin{aligned} &a, b, c, d, e, f \sim Uniform[-15,15] \\ &\theta \sim Exponential(1) \end{aligned} \tag{5.12}$$

The form of the mean and covariance functions are set as general as possible as we test our estimation framework. The prior PDFs can be specifically chosen to incorporate any knowledge we may have on the values of the unknown parameters or can be left sufficiently vague in the absence of such information. Using 500 realizations of the given random process that are sampled at the given locations, we generate the joint posterior distribution of the parameters and pick 1000 samples from it by using the Markov Chain Monte Carlo (MCMC) method with a burn-in of 30,000 and a thinning factor of 10.[25] The open-source Bayesian analysis package PyMC[26] is used to perform Monte Carlo sampling in order to estimate their posterior PDFs. The given parameters and the corresponding estimated parameters are shown in Table 5.1. The result shows that the Bayesian inference framework can estimate the parameters in the mean and covariance functions accurately by using 500 realizations.

Table 5.1 The given and estimated parameters for test problem.

Parameter	Actual Value	Estimated Value
θ	0.2	0.199±0.0003
a	-5	-4.992±0.0012
b	0	8.563e-6±0.0074
c	-3	-2.998±0.0012
d	0	0.002±0.0011
e	0	0.000±0.0021
f	5	4.991±0.0088

5.3.5 Sample size determination for GP parameter estimation

As commonly known, the bigger sample size is always preferred for the higher probability of finding a significant result.[27] However, a large sample size is not always obtainable in the experiment: sometimes, the number of samples is limited in size because of the limit of resources, a small research population, ethical issues, and so on. Therefore, the number of sample size that can produce statistically meaningful results needs to be studied. Additionally, this number should be informed to the experimentalist, so that he can plan the experiment.

The number of realizations changes from 500 to 20 and the accuracy of the mean of estimated parameters are plotted in Figure 5.13 (a). The X-axis is the number of realizations that is used for the parameter estimation, and the Y-axis stands for the normalized estimated parameters by its true value. The legend shows the parameters to be estimated. As the realization size decreases, it deviates from its true value and the error becomes ~10 % of its true value when 20 realizations are used. Less than 50 realizations gives a large deviations from its true value (more than 5 %). Figure 5.13 (b) shows the trend of standard deviation of estimated parameters. As the number of realizations decreases, the standard deviation of estimated parameter increases, meaning there exists more chance to estimate the parameter values with a large error: the estimated uncertainty increases.

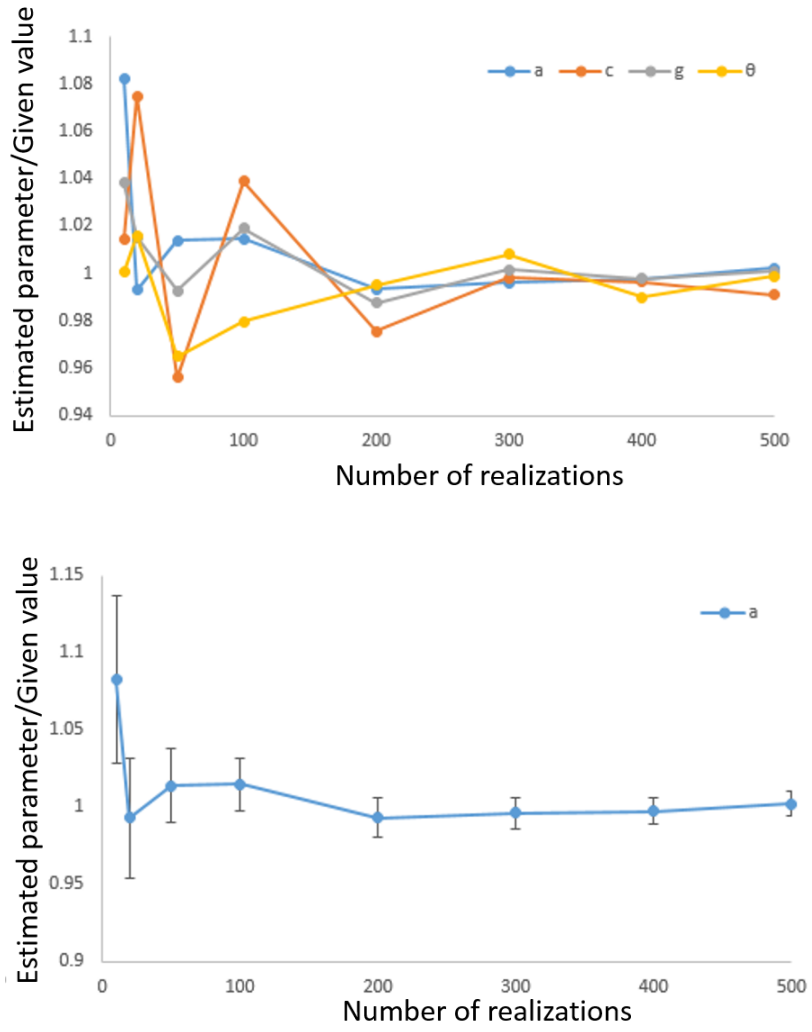

Figure 5.13 The mean (a) and the standard deviation (b) of the estimated parameters normali zed by given values vs. the number of realizations used in the estimation. As the number of r ealizations decreases, the accuracy of mean of estimation reduces and the standard deviation of estimation increases.

We confirm that this result is consistent with the conclusion that is made by Lee and Song,[28] saying the maximum likelihood estimator requires at least 5 times larger sampling size than the number of parameters to be estimated. In our case, the number of parameters to be estimated is 7, therefore, more than 35 samples need to be considered in the estimation.

The numbers are not exact for all cases because it depends on the model, distribution of the parameters and other characteristics of the problem, but this can be a guideline for planning the experiment.

5.4 Conclusion

This work suggests a novel modeling framework with uncertainty quantification that helps to understand the distribution of the mechanical property of die casting products. The proposed framework consists of the computational approach that can connect the input parameters with final product quality through the manufacturing process modeling. Within this framework, a novel characterization method that can extract the microstructural information (e.g. grain size) from experimental micrographs is developed. Additionally, the calibration/validation framework with the Gaussian process is utilized to increase the reliability of computational model. This work suggests a framework that can model the stochasticity of microstructure by including the Gaussian process modeling with Bayesian inference. The verification process shows that the Bayesian estimation framework can capture the proper parameter values from the realizations of the given Gaussian process model. The proposed framework provides a general methodology that helps to calibrate and validate the computational model that simulates the entire manufacturing processes with uncertainties.

5.5 References

1. North America Die Casting Association Homepage. http://www.diecasting.org/

2. Underwood, E. E., Quantitative stereology for microstructural analysis. In *Microstructural Analysis*, Springer: 1973; pp 35-66.

3. (a) Furukawa, M.; Horita, Z.; Nemoto, M.; Valiev, R.; Langdon, T., Microhardness measurements and the Hall-Petch relationship in an Al Mg alloy with submicrometer grain size. *Acta Materialia* **1996,** *44* (11), 4619-4629; (b) Tachibana, S.; Kawachi, S.; Yamada, K.; Kunio, T., Effect of grain refinement on the endurance limit of plain carbon steels at various strength levels. *Trans. Jpn. Soc. Mech. Eng.,(in Japanese)* **1988,** *54* (507), 1956-1961; (c) Berbenni, S.; Favier, V.; Berveiller, M., Impact of the grain size distribution on the yield stress of heterogeneous materials. *International Journal of Plasticity* **2007,** *23* (1), 114-142; (d) Chapetti, M.; Miyata, H.; Tagawa, T.; Miyata, T.; Fujioka, M., Fatigue strength of ultra-fine grained steels. *Materials Science and Engineering: A* **2004,** *381* (1), 331-336.

4. ASTM, E112–96. *Standard Test Methods for Determining Average Grain Size. ASTM International* **2004**.

5. ASTM, E1382–97. *Standard Test Methods for Determining Average Grain Size Using Semiautomatic and Automatic Image Analysis*. *ASTM International* **2004**.

6. (a) Lehto, P.; Remes, H.; Saukkonen, T.; Hänninen, H.; Romanoff, J., Influence of grain size distribution on the Hall–Petch relationship of welded structural steel. *Materials Science and Engineering: A* **2014,** *592*, 28-39; (b) Lehto, P.; Romanoff, J.; Remes, H.; Sarikka, T., Characterisation of local grain size variation of welded structural steel. *Welding in the World* **2016,** *60* (4), 673-688.

7. Parvin, B.; Yang, Q.; Han, J.; Chang, H.; Rydberg, B.; Barcellos-Hoff, M. H., Iterative voting for inference of structural saliency and characterization of subcellular events. *IEEE Transactions on Image Processing* **2007,** *16* (3), 615-623.

8. Miodownik, M. A., A review of microstructural computer models used to simulate grain growth and recrystallisation in aluminium alloys. *Journal of Light Metals* **2002,** *2* (3), 125-135.

9. Qian, M.; Cao, P.; Easton, M.; McDonald, S.; StJohn, D., An analytical model for constitutional supercooling-driven grain formation and grain size prediction. *Acta materialia* **2010,** *58* (9), 3262-3270.

10. Kennedy, M. C.; O'Hagan, A., Bayesian calibration of computer models. *Journal of the Royal Statistical Society: Series B (Statistical Methodology)* **2001,** *63* (3), 425-464.

11. Schalkoff, R. J., *Digital image processing and computer vision*. Wiley New York: 1989; Vol. 286.

12. Forsyth, D.; Ponce, J., *Computer vision: a modern approach*. Upper Saddle River, NJ; London: Prentice Hall: 2011.

13. Singh, T. R.; Roy, S.; Singh, O. I.; Sinam, T.; Singh, K., A new local adaptive thresholding technique in binarization. *arXiv preprint arXiv:1201.5227* **2012**.

14. Greer, A.; Bunn, A.; Tronche, A.; Evans, P.; Bristow, D., Modelling of inoculation of metallic melts: application to grain refinement of aluminium by Al–Ti–B. *Acta materialia* **2000,** *48* (11), 2823-2835.

15. Aaron, H. B.; Fainstein, D.; Kotler, G. R., Diffusion-Limited Phase Transformations: A Comparison and Critical Evaluation of the Mathematical Approximations. *Journal of applied physics* **1970,** *41* (11), 4404-4410.

16. Easton, M.; StJohn, D., Improved prediction of the grain size of aluminum alloys that includes the effect of cooling rate. *Materials Science and Engineering: A* **2008,** *486* (1), 8-13.

17. Raeisinia, B.; Sinclair, C., A representative grain size for the mechanical response of polycrystals. *Materials Science and Engineering: A* **2009,** *525* (1), 78-82.

18. Tschopp, M.; Wilks, G.; Spowart, J., Multi-scale characterization of orthotropic

microstructures. *Modelling and Simulation in Materials Science and Engineering* **2008,** *16* (6), 065009.

19. Benati, D. M.; Zoqui, E. J., Effect of Silicon on the Thixoformability of Al-Si-Cu Alloys. *Journal of materials engineering and performance* **2014,** *23* (9), 3165-3179.

20. Dixon, W. J.; Massey Frank, J., *Introduction To Statistical Analsis*. McGraw-Hill Book Company, Inc; New York: 1950.

21. Chan, T. F.; Vese, L. A., Active contours without edges. *IEEE Transactions on Image Processing* **2001,** *10* (2), 266-277.

22. Qi, X.; Xing, F.; Foran, D. J.; Yang, L., Robust segmentation of overlapping cells in histopathology specimens using parallel seed detection and repulsive level set. *IEEE Transactions on Biomedical Engineering* **2012,** *59* (3), 754-765.

23. Giachetti, A.; Lovato, C. In *Radial symmetry detection and shape characterization with the multiscale area projection transform*, Computer Graphics Forum, Wiley Online Library: 2012; pp 1669-1678.

24. Rowenhorst, D.; Gupta, A.; Feng, C.; Spanos, G., 3D crystallographic and morphological analysis of coarse martensite: combining EBSD and serial sectioning. *Scripta Materialia* **2006,** *55* (1), 11-16.

25. Alwan, A.; Aluru, N., Data-driven stochastic models for spatial uncertainties in micromechanical systems. *Journal of Micromechanics and Microengineering* **2015,** *25* (11), 115009.

26. Patil, A.; Huard, D.; Fonnesbeck, C. J., PyMC: Bayesian stochastic modelling in Python. *Journal of statistical software* **2010,** *35* (4), 1.

27. Peto, R.; Pike, M.; Armitage, P.; Breslow, N.; Cox, D.; Howard, S. V.; Mantel, N.; McPherson, K.; Peto, J.; Smith, P., Design and analysis of randomized clinical trials requiring prolonged observation of each patient. I. Introduction and design. *British journal of cancer*

1976, *34* (6), 585-612.

28. Lee, S.-Y.; Song, X.-Y., Evaluation of the Bayesian and maximum likelihood approaches in analyzing structural equation models with small sample sizes. *Multivariate Behavioral Research* **2004,** *39* (4), 653-686.